

# **The Search for Double Internal Conversion in $^{137m}\text{Ba}$**

**Jackson T. H. Dowie**

A thesis submitted for the degree of  
Bachelor of Science with Honours in Physics of  
The Australian National University

**October, 2016**



---

# Declaration

---

This thesis is an account of research undertaken between February 2016 and October 2016 at The Department of Nuclear Physics, Research School of Physics and Engineering, The Australian National University, Canberra, Australia.

Except where acknowledged in the customary manner, the material presented in this thesis is, to the best of my knowledge, original and has not been submitted in whole or part for a degree in any university.

---

Jackson T. H. Dowie

October, 2016



---

## Acknowledgements

---

First, I like to thank my supervisor, Tibor Kibédi. He has been an incredible help and integral to the completion of this project. Tibor's knowledge, insight and assistance have been deeply appreciated. I also need to thank Andrew Stuchbery whose assistance has been invaluable. Matthew Reed has been a great help throughout the year especially with the experiment. I'd also like to thank Tim Gray for always being ready to lend a helping hand or ear. I'd like to extend my gratitude to Mitchell de Vries, Tomas Erikson, and Ben Coombes who helped with the experiment.



---

# Abstract

---

Double internal conversion is a theoretically predicted second-order electromagnetic decay pathway in nuclear decay. Although the theoretical description for double internal conversion is mature, there have been no calculations of the expected properties of the process in the literature. A number of indirect measurements through the observation of X-rays attributed to double electron ejection in nuclear decay have been made. However, the contribution and significance of the double internal conversion process is unknown and no conclusive experimental observation of the process has been made.

The theoretical description of double internal conversion has been extended for the calculation of the double differential cross section of the double internal conversion process, the transition probability with respect to the energies and angles of the emitted electrons. For the case of the 662 keV transition of  $^{137m}\text{Ba}$ , the double differential cross section, the energy distribution and total transition rate of the double internal conversion process has been calculated for the first time. The calculated value for the rate of double internal conversion to single conversion in  $^{137m}\text{Ba}$  is  $P_{KK}/P_K = 1.315 \times 10^{-6}$ .

The theoretical model was used to characterise the efficiency of the Superconducting electron spectrometer (Super-e) here at the ANU to double internal conversion and an experimental investigation into double internal conversion in the decay of  $^{137m}\text{Ba}$  was undertaken. We were unable to obtain an experimentally derived rate but we were able to obtain an independent experimental limit on the process. This limit is  $P_{KK}/P_K$  of  $20.8 \times 10^{-5}$ . The current experimental setup prevents direct observation but the theoretical prediction agrees with the experimental limit.



---

# Contents

---

<b>Declaration</b>	<b>iii</b>
<b>Acknowledgements</b>	<b>v</b>
<b>Abstract</b>	<b>vii</b>
<b>1 Introduction and Motivation</b>	<b>1</b>
<b>2 Background</b>	<b>3</b>
2.1 Nuclear States and the Electromagnetic Interaction . . . . .	3
2.1.1 Mono-Quantum Decay types . . . . .	4
2.1.2 Two-Quantum Transitions . . . . .	5
2.2 Alternative Double K-Shell Electron Ejection Processes . . . . .	7
2.2.1 Shake Off . . . . .	8
2.2.2 Direct Collision . . . . .	9
2.2.3 Internal Conversion of Internal Compton Effect . . . . .	9
2.3 Experimental Background on Second-Order Electromagnetic Processes . . . . .	9
2.4 Decay of $^{137}\text{Cs}$ and $^{137m}\text{Ba}$ . . . . .	11
2.5 Open Questions and Objectives of the Project . . . . .	12
<b>3 Theoretical Model for Double Internal Conversion</b>	<b>15</b>
3.1 Theoretical Model . . . . .	15
3.1.1 Electron States . . . . .	15
3.1.2 Nuclear States . . . . .	16
3.1.3 Probability of the Double Internal Conversion Process . . . . .	16
3.1.4 Angular Dependence . . . . .	17
3.1.5 Interaction Hamiltonian . . . . .	18
3.1.6 Reduced Two Quantum Transition Matrices . . . . .	20
3.1.7 Partial Internal Conversion Coefficients . . . . .	20
3.1.8 Selection Rules for Conversion Electrons . . . . .	21
3.1.9 Angular Separation Function . . . . .	21
3.2 Program Development . . . . .	22
3.3 Application to $^{137m}\text{Ba}$ . . . . .	23
3.4 Theoretical Predictions of Double Internal Conversion in $^{137m}\text{Ba}$ . . . . .	25
3.5 Comparison to Alternative KK Processes . . . . .	27
<b>4 Experimental Apparatus</b>	<b>33</b>
4.1 Spectrometer design . . . . .	33
4.2 Magnetic selection . . . . .	35
4.3 Super-e efficiency . . . . .	36
4.4 Momentum selection . . . . .	37

---

<b>5 Data Analysis</b>	<b>39</b>
5.1 Event-by-Event Data . . . . .	39
5.2 Energy Gain Matching . . . . .	39
5.3 Time Difference Matching . . . . .	40
5.4 $B/B\rho$ Selection . . . . .	40
5.5 Time Prompt Selection . . . . .	41
5.6 Background Subtraction . . . . .	42
<b>6 Experimental Procedure</b>	<b>45</b>
<b>7 Experimental Results</b>	<b>47</b>
<b>8 Conclusion and Outlook</b>	<b>51</b>
8.1 Conclusion . . . . .	51
8.2 Future Direction . . . . .	52
<b>Bibliography</b>	<b>53</b>

---

# List of Figures

---

2.1	Feynman diagram of gamma ray emission [5] . . . . .	4
2.2	Feynman diagrams of two quantum de-excitation processes [5]. . . . .	6
2.3	Energy spectrum of emitted electrons of accompanying processes to conversion electron emission [16]. . . . .	8
2.4	The decay scheme of $^{137}\text{Cs}$ . . . . .	11
3.1	Feynman diagrams depicting the four possible pathways for double internal conversion. . . . .	19
3.2	Possible decay paths of the two-photon decay from the $1h_{11/2^-}$ neutron hole state to the $2d_{3/2^+}$ ground state through intermediate neutron hole states (left-hand side). On the right hand side the neutron configuration in the independent particle model of the $1h_{11/2^-}$ state is shown. A transition through the $1g_{9/2^+}$ state is allowed (red arrow). On the other hand an excitation from a neutron to the $2f_{7/2^+}$ -state is not possible (blue arrow), since there is no one-step de-excitation back to the $2d_{3/2^+}$ ground state. [5].	23
3.3	Figure showing the lowest lying excited state of $^{137}\text{Ba}$ above the 662 keV state. It is a valid intermediate state in the M2E2 decay pathway [4]. . . . .	24
3.4	The double differential cross section of the E1M3+M3E1 two quantum process. . . . .	27
3.5	The double differential cross section of the E2M2+M2E2 two quantum process. . . . .	28
3.6	The double differential cross section of the E3M1+M1E3 two quantum process. . . . .	29
3.7	Double differential cross section with respect to separation angle an electron energy for the total double internal conversion process in the decay of $^{137m}\text{Ba}$	30
3.8	Plot of expected energy spectrum of K shake off electrons accompanying K conversion electron from $^{137}\text{Ba}$ [15] . . . . .	31
3.9	Plot of theoretical KK double internal conversion energy spectrum for the 662 keV M4 transition of $^{137}\text{Ba}$ . . . . .	32
4.1	Radial cross section of the Super-e. The baffles are shown in crosshatching, the source position is the green dot at the origin of the axes, the Miel detector array is represented in pink with the active detector segments displayed in yellow . . . . .	33
4.2	Picture of the Miel detector array. The HeavyMet strips are labelled and the six detectors are visible between the separating dividers. . . . .	34
4.3	Illustration of the behaviour of charged particles inside the Super-e. The two electrons are transported by the magnetic field to the detector past the baffle system. . . . .	35

5.1	Plot of the Energy - $B/B\rho$ plane. The region of legitimate events is within the horizontal band. Plot of the $B/B\rho$ spectrum, those legitimate events are visible as a large peak above the continuous background. The limiting values of $B/B\rho$ can be determined from the edges of the peak. . . . .	41
5.2	This is an example of a time difference spectrum where the central peak corresponds to events from time correlated processes while the broad flat wings are formed by the random background. . . . .	42
7.1	Plot of the gamma ray spectrum and collected conversion electron spectrum at a current setting of 3.10 A. . . . .	47
7.2	Plot of the gamma ray spectrum and collected double internal conversion electron spectrum at a current setting of 1.96 A. The vertical red line denotes 587 keV, the expected peak location for K-shell double conversion events. The fitted background spectrum is plotted in black over the experimental spectrum. . . . .	48

---

# List of Tables

---

2.1	Gamma-ray ( $\gamma$ ) and single conversion electron (CE) emission rates of the 661.660 keV transition in $^{137}\text{Ba}$ . . . . .	11
2.2	Experimental data on second order EM emission rates. . . . .	13
3.1	Table of the spin and parity assignment of the intermediate nuclear states accessed by each two quantum pathway . . . . .	24
3.2	Table of the transition strengths of each multipole combination [4]. . . . .	25
3.3	Table of the various electron states accessed by different electromagnetic transitions. . . . .	26

# Introduction and Motivation

---

The electromagnetic interaction is the most well understood of the four fundamental forces. It is an almost perfect probe of nuclear structure, strong enough to effect observable changes in the nuclear charge and current distributions but weak enough to be understood in the context of perturbation theory. [1]

Second-order electromagnetic nuclear decay processes are predicted by our current understanding of the electromagnetic interaction, however direct experimental verification of the theoretical correctness of higher-order processes is extremely sparse. [2]

Indeed, due to the complexities of the second order electromagnetic nuclear decay processes, theoretical estimates for these processes in terms of decay rates and energy and angular distributions have also been lacking. [3]

Recent work by Christopher Walz et al. [4] on the 662 keV M4 transition in  $^{137}\text{Ba}$  has determined the transition rate for the double gamma decay process, the fundamental second order decay process. In addition, comprehensive theoretical calculations have been done to characterise our current theoretical understanding of double gamma decay in  $^{137}\text{Ba}$ .

In light of this recent work, the experimental and theoretical gaps in the knowledge of second-order electromagnetic decay processes, and apparatus here at the ANU, this thesis seeks to characterise the double internal conversion process in the 662 M4 transition in  $^{137}\text{Ba}$ .

Our current experimental and theoretical understanding of second order decay processes, especially double internal conversion is reviewed, followed by comprehensive theoretical calculations of the double internal conversion process, estimating the total rate, and energy and angular distributions. The experiment undertaken to observe double internal conversion will be described and the results will be discussed in this work.

In summary the brief of this project was to:

- develop the necessary theory of double internal conversion (at the interface of atomic and nuclear physics) to evaluate the double differential cross section (as a function of energy and angle) which has not been given explicitly in the literature,
- calculate the theoretical predictions of the double internal conversion process for the first time in the case of  $^{137m}\text{Ba}$ ,
- develop a computer program based on the theory furthered by this work so that the

efficiency of the Super-e with respect to double internal conversion can be characterised,

- develop the ANU super-e spectrometer to detect double internal conversion decay,
- perform measurements on  $^{137m}\text{Ba}$  seeking double internal conversion decay,
- develop data analysis techniques specific to double internal conversion for use with the Super-e,
- resolve conflicting claims in the literature about the probability for double internal conversion relative to single conversion in  $^{137m}\text{Ba}$ .

---

# Background

---

## 2.1 Nuclear States and the Electromagnetic Interaction

The nucleus is composed of a collection of nucleons (protons and neutrons) held together by the strong force. The nucleons interact with each other and form arrangements or states with particular values of energy, angular momentum or spin, and parity.

Nuclear state energy, or excitation energy, is generally measured from the ground state, which for a given nuclide is the lowest possible energy arrangement of those nucleons, which is defined as zero energy.

It is important to note that electromagnetic transitions change the distributions of protons and neutron inside a nucleus but they do not change the number of each kind of nucleon.

Nuclei decay down to the ground state from any excited state through a series of electromagnetic transitions corresponding to changes in the charge and current distributions in the given nucleus. These transitions have a particular energy, multipolarity or angular momentum, and parity associated with them, corresponding to the changes in energy, parity and angular momentum of the nuclear states.

The multipolarity,  $L$ , of a transition obeys the quantum mechanical selection rules for angular momentum. So for initial and final angular momentum states,  $I_i$  and  $I_f$ , we have  $|I_i - I_f| \leq L \leq |I_i + I_f|$ .

Electromagnetic transitions can either have an Electric, E, or a Magnetic, M, character. This character depends on how the transition took place, i.e. what changes are taking place in the distribution of charges and currents inside the nucleus. The parity of an electromagnetic transition depends on the multipolarity and character of a transition, specifically with the parity,  $\pi$ , of a transition is given by  $\pi = (-1)^{L+S}$  where  $S = 1$  for Magnetic transitions and  $S = 0$  for electric transitions.

The electromagnetic transitions proceed via the emission of quanta which mediate the change in the energy, angular momentum and parity of the nucleus.

The interaction between the nucleus and the electromagnetic field can be described by Equation 2.1 in the non-relativistic approximation [5]:

$$H_{int} = \int j_\mu(x) A^\mu(x) d^3x + \frac{1}{2} \int B_{\mu\nu}(x, y) A^\mu(x) A^\nu(y) d^3x d^3y \quad (2.1)$$

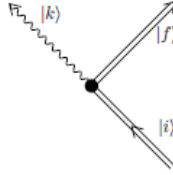


**Figure 2.1:** Feynman diagram of gamma ray emission [5]

Equation 2.1 is written in gaussian units where  $\hbar = c = 1$  and  $\alpha = e^2$ .  $j_\mu(x) = (\rho(x), \mathbf{j}_\mu)$  is the nuclear current operator and  $A^\mu(x)$  is the electromagnetic vector potential.  $B_{\mu\nu}(x, y)$  is the ‘seagull’ operator which represents the sum over very high mass states consisting of virtual nucleon-antinucleon pairs in the full relativistic treatment [6].

Electromagnetic decays are analysed in terms of perturbation theory [1]. Treating the first term of the Hamiltonian expressed in Equation 2.1 in first order perturbation theory, one obtains the equations for single quantum decay processes.

Taking the first term,  $\int j_\mu(x)A^\mu(x)d^3x$  to the second order and taking the second term,  $\int B_{\mu\nu}(x, y)A^\mu(x)A^\nu(y)d^3xd^3y$ , to the first order, one obtains the equations for two quantum nuclear transitions.

### 2.1.1 Mono-Quantum Decay types

Taking the first term of the interaction Hamiltonian to the first order generates the single quantum equations. A nucleus has three possible decay pathways in a single quantum context. They are gamma-ray emission, internal conversion, and internal pair formation.

#### Gamma-Ray Emission

Gamma ray emission is the fundamental electromagnetic decay mode. It involves the emission of a photon which carries away the energy and angular momentum for the transition. The energy of the quantum of radiation is that of the full energy of the nuclear transition.

The process can be described by the Feynman diagram shown in Figure 2.1. It depicts the nucleus moving from the initial state to the final state, via the emission of a photon [5]. This represents the most fundamental of the nuclear interactions with the electromagnetic field.

#### Internal Conversion

Internal conversion is a nuclear decay process in which the nucleus moves from an excited state to a less excited state by interacting with one of the orbital electrons. The energy of the transition is given to an orbital electron and the electron is ejected from the atom. The energy of the emitted electron is that of the nuclear transition minus the atomic binding energy. The emitted electrons form sharp discontinuous lines in an energy spectrum, unlike the broad continuous distribution of  $\beta$  rays [1].

It is important to note that internal conversion is not the emission of a gamma ray from the nucleus and its subsequent absorption by an orbital electron. Instead, internal conversion is the direct interaction of the nucleus and an electron mediated by the nearby electromagnetic field of the nucleus [1].

The greater the electron wavefunction overlap with nucleus and the nuclear electromagnetic field, the greater the probability of internal conversion. Therefore, internal conversion proceeds more with electrons in shells closer to the nucleus such as electrons in the K shell.

Internal conversion probability increases with increasing atomic number or  $Z$ , increasing multipolarity of the nuclear transition, decreasing transition energy, and is more likely to occur in a magnetic transition than in an electric transition, at least at lower energies. With increasing energy, the difference in conversion rates disappears [1].

An important feature of internal conversion is that it can proceed through E0 transitions which are impossible for normal gamma-ray emission as a photon must have a non-zero value for the orbital angular momentum.

The process of internal conversion can be represented in the same manner as Figure 2.1 with the emitted quanta instead being virtual and interacting with an orbital electron.

The rate of internal conversion is described by the internal conversion coefficient. It is defined to be the ratio of nuclear decays by internal conversion to the number of nuclear de-excitations by gamma-ray emission. Often the internal conversion coefficient is defined for the rates of internal conversion of electrons from each electronic shell. For example one can have the K conversion coefficient; the conversion coefficient defining the rate of ejection of K shell electrons compared to the rate of gamma decay.

### Internal Pair Formation

Internal pair formation is a single quantum decay pathway wherein the nucleus de-excites through the creation and emission of an electron-positron pair instead of the emission of an photon or ejection of an orbital electron. This decay pathway is only available when the nuclear transition has energy greater than 1.022 MeV, or two times the rest mass energy of an electron. In this kind of transition, the sum of the kinetic energies of the two charged particles plus the rest mass energy of the emitted electron and positron equals the total energy in the nuclear transition [7].

#### 2.1.2 Two-Quantum Transitions

Two quantum transitions are second order electromagnetic processes. They are predicted to occur according to electromagnetic theory but experimental evidence of their existence and evidence of the accuracy of the theoretical predictions is scarce. Two quantum transitions have been investigated by many authors [8, 9, 10, 11, 12, 6, 5].

The two quantum decay processes work by the coupling of the initial nuclear state to the final state through all appropriate excited states of the nucleus. In two-quantum transitions, the single transition is decomposed into two virtual transitions, in which the total parity change and angular momentum change is preserved by the sum of the changes from the two transitions. The two virtual electromagnetic transitions couple between the

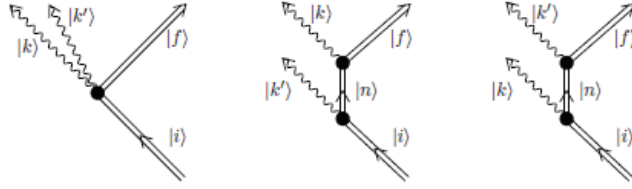


**Figure 2.2:** Feynman diagrams of two quantum de-excitation processes [5].

initial and final nuclear states through a set of excited states of the nucleus. The two transitions obey the quantum mechanical selection rules with regard to the total angular momentum change of the whole nuclear transition,  $|L_1 + L_2| \geq L$ . In general, though, only those pairs of virtual transitions with  $|L_1 + L_2| = L$  are significant. It is important to note that the intermediate states the process moves through are real excited states of the nucleus. The process is therefore highly dependent on the structure of the nucleus. The total two-quantum transition rate is composed of the sum of the contributions from every possible combination of two single virtual transitions through all the appropriate intermediate excited states, i.e. those excited states that have the correct spin and parity for the pair of electromagnetic transitions.

We can represent these two quantum transitions via the three Feynman diagrams depicted in Figure 2.2. The first diagram represents the effect of the second term in the Hamiltonian expressed in Equation 2.1. The following two diagrams represent the movement of the nucleus through intermediate states and correspond to the second-order perturbation of the first term of the Hamiltonian.

According to Grechukhin [12], the second or quadratic term of the Hamiltonian has a negligible effect on these two-quantum processes. According to Kramp [6], the quadratic term is only significant in two-quantum decays proceeding via two virtual magnetic transitions. Transitions which precede via two virtual magnetic transitions are not of interest in this work because the transition of interest is an  $M4$  transition which in order to preserve parity change, can only proceed via pairs of virtual transitions which include both an Electric and Magnetic transition.

The key characteristic of two-quantum decay processes in nuclei is the emission of two quanta. The energies of the two quanta form a continuous distribution. However, the sum of the energies associated with each quantum add to the full energy of the transition.

Theoretical estimates for decay probabilities of two quantum transitions are difficult to calculate as the process depends on the sum of interactions from every appropriate excited state of the nucleus in question. The rates depend very strongly on the nuclear structure of the nuclei and rely on accurate and comprehensive nuclear models.

### Double Gamma Emission

Double gamma emission is a two-quantum decay process wherein the nucleus de-excites through the emission of two gamma rays. Energies of the two gamma rays are distributed continuously with the sum of the gamma-ray energies equaling the energy of the nuclear transition.

Double gamma emission has been theoretically studied by many authors over the years, [8, 9, 10, 6, 5]. The Feynman diagrams for the process are the same as those depicted in Figure 2.2.

### Gamma - Conversion Process

Another two-quantum decay process is the gamma-conversion process. This is similar to double gamma emission however one of the quanta is a conversion electron. This process leads to the simultaneous ejection of a conversion electron and a gamma ray. It has been discussed theoretically by Grechukhin [11]. In this type of transition, the sum of the kinetic energy of the electron, the electron binding energy and the gamma-ray energy adds to the full energy of the transition.

Schematically, the process is the same as shown in Figure 2.2 however one of the quanta is converted.

### Double Internal Conversion

Double internal conversion is a two-quantum decay pathway. Like the other nuclear two-quantum decay processes, double internal conversion proceeds via intermediate nuclear states. The nucleus interacts directly with two orbital electrons, which are ejected from the atom. Again like other two quantum processes, the kinetic energies of the two electrons in addition to the binding energies of the two add together to give the total energy of the transition.

A theoretical description of double internal conversion was produced by Eichler in 1959 [8] but the first consistent theoretical description was by Grechukhin [12]. Double internal conversion is the primary topic of this work and its theoretical underpinnings will be covered in more detail in Chapter 3.

Double internal conversion is different from other dual electron ejection mechanisms due to the fact that it is a nucleus-mediated process with the nucleus transitioning through intermediate states, emitting two virtual quanta that are converted by the orbital electrons. Other two-electron ejection mechanisms work through electronic intermediate states or through some interaction between the orbital electrons. These alternative electron ejection mechanisms will be explained in more detail in Section 2.2.

There have been no consistent theoretical calculations of expected rates of double internal conversion in nuclear transitions. Typically it is assumed to be small [3, 13] even though the rates, energy and angular distributions of the process have never been calculated. This is due to the difficulty in summing over the contributions from all possible intermediate states of the nucleus. It is these properties of double internal conversion that have been calculated in this work in Chapter 3.

## 2.2 Alternative Double K-Shell Electron Ejection Processes

There are a number of competitive processes to double internal conversion that lead to the ejection of two electrons from an atom undergoing a nuclear transition, the kinetic energies

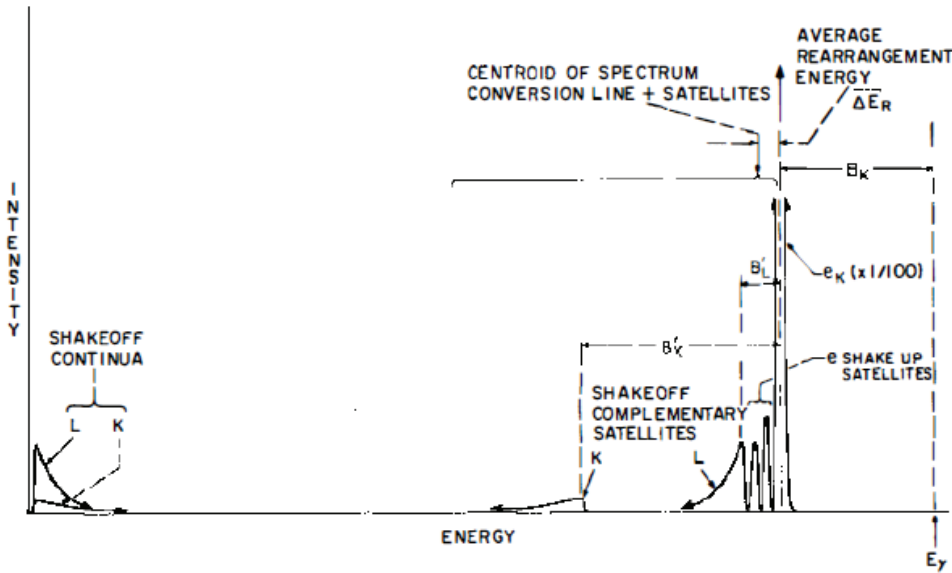


**Figure 2.3:** Energy spectrum of emitted electrons of accompanying processes to conversion electron emission [16].

of which add to the full energy of the nuclear transition minus any binding energies. They are Shake off, Direct Collision and internal conversion of internal Compton effect (ICICE).

### 2.2.1 Shake Off

During the decay of a nucleus by internal conversion, another electron can be emitted from the atom. This additional electron is ejected as a result of the sudden change in the effective nuclear charge experienced by the orbital electrons following the ejection of the conversion electron. This process is termed “Shake Off”. Shake off has been described theoretically by Mukoyama [14, 15] who has calculated the expected energy distribution of the shake off electron accompanying various kinds of conversion electron emission in addition to the total shake off rate in a range of nuclei.

Figure 2.3 depicts the typical spectrum of emitted electrons from a nuclear decay. There is a main conversion electron peak corresponding to K conversion electrons along with satellite peaks and continua corresponding to electrons emitted by different accompanying processes to internal conversion. The two electrons emitted in the shake off process share the total available energy, the energy of the nuclear transition minus the binding energies of the two emitted electrons. It is visible in Figure 2.3 that the two shake off electrons preferentially do not share the available energy equally; the contributing continua peak, with an electron at maximal energy and one at minimal energy.

Shake off appears to be the major competing process to double internal conversion with regard to the emission of two K-shell electrons [16, 15].

### 2.2.2 Direct Collision

Direct collision is another process which leads to the emission of two electrons with total energy matching that of the nuclear transition. Unlike shake off, direct collision is caused by direct interaction between the emitted conversion electron and an orbital electron. The ejected conversion electron, as it leaves the atom, interacts with an atomic electron and ionises it through the Coulomb interaction [14].

Theoretical evaluation of direct collision for internal conversion has not been done [3], but Feinberg [17] has estimated the probability of a direct collision event in K-shell electrons in comparison to shake off in K-shell electrons during  $\beta^-$  decay. The estimated relationship is

$$P(DC)/P(SO) \approx BE/KE$$

where  $P(DC)$  is the rate of direct collision events,  $P(SO)$  is the rate of shake off events,  $BE$  is the binding energy of the scattered electron and  $KE$  is the kinetic energy of the colliding electron.

Using this estimation, it suggests that direct collision is an unimportant process compared to shake off except when the transition energy is small compared to the binding energy of the orbital electrons [14].

### 2.2.3 Internal Conversion of Internal Compton Effect

Internal conversion of internal Compton effect or ICICE is a process where a real emitted gamma-ray Compton scatters off an orbital electron, ejecting it from the atom, and then is internally converted, ejecting a subsequent electron from the atom [3]. The probability of the process occurring has been suggested by Listengarten [18] to be

$$P_{KK}(ICICE) = \frac{4\alpha}{3\pi} W \int_{BE}^{W-BE} \frac{\alpha(E1, E)}{2E} dE$$

where  $P_{KK}(ICICE)$  is the probability of the process occurring,  $W$  is the nuclear transition energy,  $BE$  is the binding energy of the electron and  $\alpha(E1, E)$  is the conversion coefficient of an  $E1$  dipole radiation of energy  $E$ .

This suggestion has been found to be of limited utility in predicting rates of double K shell electron ejection in nuclear decays as it gives typically gives values for the K shell double ejection 5-7 times larger than the experimental observation of double K shell vacancy rates [3].

## 2.3 Experimental Background on Second-Order Electromagnetic Processes

Experimental investigations in second order electromagnetic processes have been tabulated in Table 2.2. There have been attempts to observe both the double gamma process and

the double internal conversion process in a variety of nuclei.

Double photon emission has been primarily observed in the non-competitive aspect, double photon emission in transitions between  $0^+$  states wherein single gamma emission is forbidden due to angular momentum selection rules. This is visible in the table with successful observation of double gamma emission in the first excited  $0^+$  to the ground  $0^+$  state transitions in  $^{16}\text{O}$ ,  $^{40}\text{Ca}$ , and  $^{90}\text{Zr}$ . The only successful cases of observing competitive double gamma emission is in  $^{137}\text{Ba}$ .

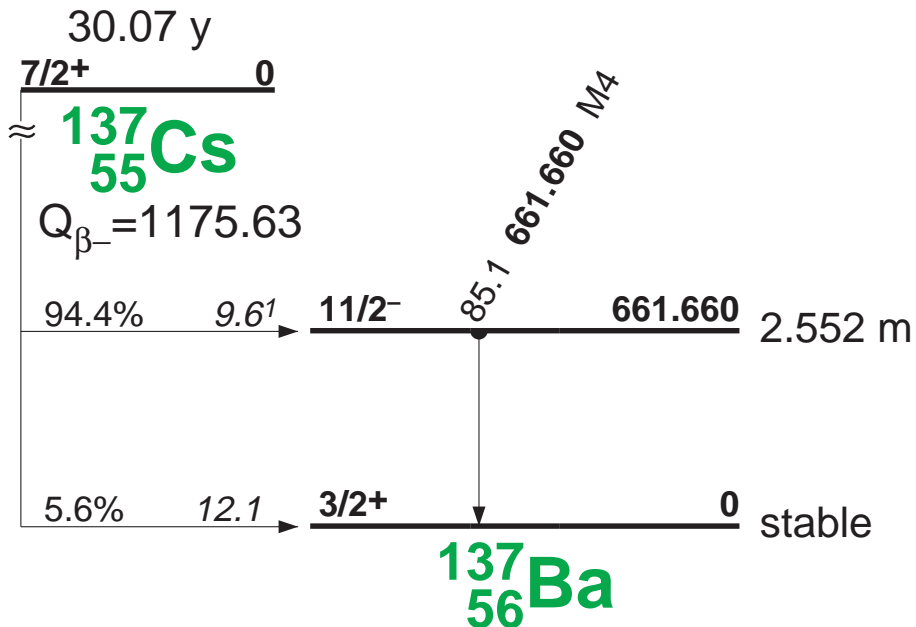
There have been a wide range of investigations into double K-shell ionisation in nuclear transitions. The commonly used tool is looking at the X-rays produced when the K-shell vacancies are filled by the other orbital electrons. Direct Electron measurements using bare particle detectors have been undertaken and so have measurements using magnetic lens spectrometers.

Measurements involving the detection of electrons are looking for coincidence events, the detection of two electrons with a narrow time window, and looking for a peak in the summed energy spectrum at an energy value corresponding to the transition energy minus the sum of the binding energies of the emitted electrons. Magnetic lens spectrometers are used in an attempt to only select out events of interest and so avoid the background such as that produced by the competing gamma-ray emission process.

X-ray coincidence measurements were made by resolving coincidence events between the X-rays emitted when the two K shell atomic vacancies were filled. One X-ray is the Hypersatellite X-ray,  $K^H$ , corresponding to the change from  $1s^{-2}$  to  $1s^{-1}2p^{-1}$ . The other X-ray is the secondary satellite X-ray,  $K^S$  which corresponds to the change from  $1s^{-1}2p^{-1}$  to  $2p^{-2}$ . These emitted X-rays are shifted to a higher energy compared to normal K X-rays so can be distinguished from the normal spectrum [3].

There are four possible processes which produce the same final state: an atom with two vacancies in the K shell and two ejected K shell electrons, whose total energy is that of the transition. All processes are competing and it is difficult to resolve each component. Many measurements of double K shell vacancy in isomeric transitions will measure the total rate of these four double K shell ionisation processes: double internal conversion, shake off, direct collision, and ICICE, with shake off probably predominant [16]. The contribution of the double internal conversion process to the total rate of double K-shell ionisation is largely unknown.

The energy spectra of the shake off, direct collision and ICICE processes are strongly weighted towards unequal energy sharing, with the secondary electron emitted at a low energy. It is conceivable that selectively viewing a distribution of electrons whose energies are equally shared would preferentially select for electrons emitted by double internal conversion which is expected to have a continuous distribution over the whole range of energy values [16]. However, in order to determine this, one would need to calculate the energy distribution and total rate of double internal conversion in an isomeric transition which, heretofore, has not been done. Section 3.1 of this work covers the first such calculations of the double internal conversion process for the 662 keV M4 transition of  $^{137m}\text{Ba}$ .

**Figure 2.4:** The decay scheme of  $^{137}\text{Cs}$ .

Transition	Energy [keV]	Emission probability
$\gamma$ -rays	661.66	0.8876
CE-K	624.22	0.0915
CE-L	658.78	0.01648
CE-M	660.41	0.00352
CE-Total	-	0.1124

**Table 2.1:** Gamma-ray ( $\gamma$ ) and single conversion electron (CE) emission rates of the 661.660 keV transition in  $^{137}\text{Ba}$ .

## 2.4 Decay of $^{137}\text{Cs}$ and $^{137m}\text{Ba}$

Fig 2.4 shows the decay scheme of  $^{137}\text{Cs}$ . The  $7/2^+$  ground state of  $^{137}\text{Cs}$  decays via two beta branches. 94.4% of the time the 661.660 keV  $J^\pi = 11/2^-$  is populated, which decays to the  $J^\pi = 3/2^+$  ground state of  $^{137}\text{Ba}$ . This transition is highly retarded as it involves a change of 4 units of angular momentum. The  $J^\pi = 11/2^-$  state is a well known isomeric, or metastable state with a half life of 2.55 minutes. This state is labelled  $^{137m}\text{Ba}$ . Because of the M4 multipolarity, more than 11% of the time the electromagnetic decay is mediated by internal conversion. The emission rates of the various first order electromagnetic transitions involving the emission of a single radiation are listed in Table 2.1.

Due to the long half life of the isomeric state, the emitted  $\beta^-$  particle is not in coincidence with the decay of  $^{137m}\text{Ba}$ . Because no other nuclear transition is in coincidence with the 661.66 keV transition, and it is highly converted, this M4 transition was long considered a good candidate to study the double photon and double conversion processes. As such, the two-quantum double-photon decay process has been observed, competing with the single

decay process in the decay of  $^{137m}\text{Ba}$  by Beusch in 1960, and Walz recently in 2014 and 2015 [19, 5, 4]. These workers have obtained rates of the double gamma process relative to the single gamma process of  $P_{\gamma\gamma}/P_\gamma = 6.4(31) \times 10^{-6}$  and  $P_{\gamma\gamma}/P_\gamma = 2.05(37) \times 10^{-6}$ , respectively.

The suitability of the 662 keV M4 transition in  $^{137}\text{Ba}$  in investigating two quantum processes and the recent success in the observation of the double gamma process in the decay by Walz [4] led to the selection of this transition in this work into the double internal conversion process.

## 2.5 Open Questions and Objectives of the Project

There are still a number of open questions with regard to two-quantum decay processes in nuclei and double internal conversion in particular.

The theory of double internal conversion is mature, with the modern and consistent theoretical description published by Grechukhin in 1966 [12]. However, no calculations of the expected transition rate and the angular and energy distributions have been made of any nuclear transition. As a result, double internal conversion is a largely unknown decay process. In addition, double internal conversion has never been conclusively observed experimentally. It is with the aim of resolving these open questions that this work was commenced.

The aims of this research project were to firstly complete the first calculations of the double internal conversion process, namely calculate the expected transition rate, and the predicted energy and angular distributions of the process, using the modern theory for double internal conversion [12]. This will be done through an investigation of double internal conversion in the decay of the isomeric state of  $^{137}\text{Ba}$ .

The second aim of this research project is to achieve the first experimental observation of the double internal conversion process in  $^{137m}\text{Ba}$  and compare the experimental results to the theoretical calculations.

In this thesis, the theoretical model and calculations for double internal conversion in the decay of  $^{137m}\text{Ba}$  are discussed in Chapter 3. The characterisation of the experimental apparatus used in the experiment with respect to the double conversion process is undertaken in Chapter 4. The data analysis techniques and principles used to sort and analyse the experimental data are expanded upon in Chapter 5. Details of the experimental procedure are discussed in Chapter 6 with the results of the experiment reported and discussed in Chapter 7.

Table 2.2: Experimental data on second order EM emission rates.

Nuclide	Transition	Multi Energy <sup>a</sup> [keV]	Multi polarity <sup>a</sup>	Emission	Experiment	Comment	References
<sup>12</sup> C	4430		E2	$\gamma\gamma/\gamma$		$\leq 1.7 \times 10^{-4}$	[20]
<sup>16</sup> O	6050		E0	$\gamma\gamma/\pi$		$2.5(11) \times 10^{-4}$	[21]
				$\gamma\gamma/(CE + IPF)$		$6.6(5) \times 10^{-4}$	[6]
<sup>40</sup> Ca	3350		E0	$\gamma\gamma/(CE + IPF)$		$4.5(10) \times 10^{-4}$	[22]
<sup>90</sup> Zr	1760		E0	$\gamma\gamma/(CE + IPF)$		$1.8(2) \times 10^{-4}$	[22]
<sup>109</sup> Ag	88		E3	$K - K/CE$		$15.3(24) \times 10^{-5}$	From X-ray coincidence [23]
				$K - K/CE$		$13.0(11) \times 10^{-5}$	From X-ray coincidence [24]
<sup>114</sup> In	192		M4	$K - K/CE$		$12 \times 10^{-5}$	From X-ray coincidence [25]
				$K - K/CE$		$3 \times 10^{-5}$	[26]
<sup>131m</sup> Xe	164		M4	$K - K/CE$		$11(2) \times 10^{-5}$	From X-ray coincidence [27]
<sup>137m</sup> Ba	661.615		M4	$\gamma\gamma/\gamma$		$6.4(31) \times 10^{-6}$	[19]
				$\gamma\gamma/\gamma$		$2.05(37) \times 10^{-6}$	[4]
				$K - K/CE$		$10.0(9) \times 10^{-5}$	From X-ray coincidence [3]
				$K - K/CE$		$18(5) \times 10^{-5}$	X-ray - $e^- - e^-$ coincidence, Energy range 115-472 keV [28]
				$K - K/CE$		$7.1(35) \times 10^{-5}$	From X-ray coincidence [29]
<sup>141</sup> Pr	145		M1+E2	$K - K/CE$		$3.4(3) \times 10^{-5}$	From X-ray coincidence [30]



# Theoretical Model for Double Internal Conversion

---

## 3.1 Theoretical Model

The first theoretical description for a two quantum nuclear decay processes was first produced by Eichler [8, 9]. However, the theory put together by Eichler did not take into account the interference effects between the possible reaction channels and the expression for the double internal conversion process was only approximate. The first detailed theoretical model of the second order effects, including double photon emission [10, 11, 12] and later of double electron emission [12] was presented by Grechukhin.

As part of Grechukhin's work on various two quantum phenomena, [10, 11], Grechukhin had published an equation to calculate the properties of double internal conversion. However, in the 1966 paper, [12] Grechukhin outlines the general form of the equation but only looks explicitly at the energy spectrum of double internal conversion, with no mention of the angular dependence.

In this chapter, we will explore the theoretical model put forth by Grechukhin [12] to understand the double internal conversion process. A computer program has been developed to calculate the transition probabilities for double internal conversion based on this theoretical model. The double internal conversion process in the decay of  $^{137m}\text{Ba}$  has been characterised and the results of the theoretical calculations will be discussed.

### 3.1.1 Electron States

In the model, the electron states are described by the set of quantum numbers  $j, \mu, \lambda, \epsilon$  which correspond to the total angular momentum,  $j$ ; the magnetic projection of the angular momentum,  $\mu$ ; the larger component Dirac spinor parity index,  $\lambda$ , and energy of the electron  $\epsilon$ .  $\lambda$ , the parity of the Dirac wavefunction that describes the electron, can have a value of  $+\frac{1}{2}$  or  $-\frac{1}{2}$ . It relates to the orbital angular momentum,  $l$ , of the electron state by  $l = j + \lambda$ .

These electronic states can also be defined by the Dirac quantum number,  $K$ , which relates to the orbital quantum number,  $l$ , and the total angular momentum,  $j$ , in the following

ways:

$$\begin{aligned} j &= |K| - \frac{1}{2} \\ K &= l(l+1) - (j + \frac{1}{2})^2 \end{aligned}$$

The initial electron states are indexed with the letter  $q_i$ , while the final electron states are denoted by the letter  $p_i$ .

The continuum electron states are also described by another set of quantum numbers in order to define the electronic states with regard to the direction of motion of the electrons, namely:  $\mathbf{p}, \epsilon, \sigma, \lambda$  where  $\epsilon$  and  $\lambda$  are the same as above and  $\mathbf{p}$  and  $\sigma$  are the momentum vector and spin projection of the electron along the momentum direction.

These electron states are represented by the kets:  $|q_i\rangle$  to describe an initial and  $|p_i\rangle$  to describe a final continuum electron state in the  $j, \mu, \lambda, \epsilon$  basis and  $|\mathbf{p}_i\rangle$  to describe a final continuum electron state in the  $\mathbf{p}, \epsilon, \sigma, \lambda$  basis.

### 3.1.2 Nuclear States

Likewise, the initial state of the nucleus with energy,  $E_1$ , parity,  $\Pi_i$ , angular momentum,  $I_1$ , and projection,  $M_1$ , is denoted  $|I_1 M_1 E_1 \Pi_1\rangle$  or  $|I_1\rangle$ . The final nuclear state is correspondingly defined by its energy, angular momentum, projection and parity and is denoted  $|I_2 M_2 E_2 \Pi_2\rangle$  or  $|I_2\rangle$ . Real excited intermediate states of the nucleus in the virtual two quantum transitions will be designated by a lowercase letter subscript, for example,  $|I_i M_i E_i \Pi_i\rangle$  or  $|I_i\rangle$

### 3.1.3 Probability of the Double Internal Conversion Process

The following equation gives the transition probability per unit time in units of  $m_e c^2 / \hbar$  of the conversion of two orbital electrons in states  $|q_1\rangle$  and  $|q_2\rangle$ , into continuum states of momenta  $\mathbf{p}_1$  and  $\mathbf{p}_2$ , energies  $\epsilon_1$  and  $\epsilon_2$ , and spin projections  $\sigma_{p_1}$  and  $\sigma_{p_2}$ :

$$\begin{aligned} dW(\dots [q_i]^{n_i} \dots \rightarrow \mathbf{p}_1 \sigma_{p_1} \epsilon_{p_1} \mathbf{p}_2 \sigma_{p_2} \epsilon_{p_2}) &= d\epsilon_{p_1} d\epsilon_{p_2} \delta(E_1 - E_2 - [\epsilon_{p_1} + \epsilon_{p_2} - \epsilon_{q_1} - \epsilon_{q_2}]) \\ &\quad d\Omega_{p_1} d\Omega_{p_2} 2\pi \frac{1}{2I_1 + 1} \sum_{M_1 M_2} \sum_{\alpha_i} \left| \sum_{j_{p_1} j_{p_2}} \sum_{\mu_{p_1} \mu_{p_2}} \sum_{\lambda_{p_1} \lambda_{p_2}} \right. \\ &\quad \left. \langle \mathbf{p}_1 | p_1 \rangle \langle \mathbf{p}_2 | p_2 \rangle H_{ee}([q_i]^{n_i} \rightarrow p_1 p_2 q_1 q_2) \right|^2 \end{aligned} \quad (3.1)$$

The units are Gaussian with  $\hbar = 1$ ,  $c = 1$ ,  $e^2 = \alpha$  and energy in units of  $m_e c^2$ , and the transition rate is given in units of  $m_e c^2 / \hbar$ .

The Hamiltonian,  $H_{ee}([q_i]^{n_i} \rightarrow p_1 p_2 q_1 q_2)$ , and the brackets,  $\langle \mathbf{p}_1 | p_1 \rangle \langle \mathbf{p}_2 | p_2 \rangle$  are summed over the range of possible states of the emitted conversion electrons in the  $j, \mu, \lambda, \epsilon$  basis. This summation is governed by the relationship between the possible nuclear transitions and which electronic states each can excite. This relationship is described in further

detail in Section 3.1.8. The brackets,  $\langle \mathbf{p}_1 | p_1 \rangle \langle \mathbf{p}_2 | p_2 \rangle$ , are explained in Section 3.1.4 and the Hamiltonian,  $H_{ee}([q_i]^{n_i} \rightarrow p_1 p_2 q_1 q_2)$ , is discussed further in Section 3.1.5.

The sum over  $\alpha_i$  denotes the sum over all unobservable indices of the final atomic electron states after the conversion of electrons in states  $|q_1\rangle$  and  $|q_2\rangle$  and averaging over all possible initial electron arrangements. In the case of double internal conversion for the K shell, however, this averaging is not carried out as both the initial and final states are unique.

### 3.1.4 Angular Dependence

The brackets  $\langle \mathbf{p}|p\rangle$  are the coefficients of expansion of the final state continuum electron wavefunction in the  $j, \mu, \lambda, \epsilon$  basis in terms of the  $\mathbf{p}, \epsilon, \sigma, \lambda$  basis. The continuum wavefunctions in the  $\mathbf{p}, \epsilon, \sigma, \lambda$  basis have a plane and converging spherical wave in the asymptotic expression [12]. The expansion coefficients have been given in an earlier paper by Grechukhin [31].

The  $\mathbf{p}, \epsilon, \sigma, \lambda$  states can be expressed as:

$$\Psi_{\mathbf{p}_i \epsilon_{p_i} \sigma_{p_i} \lambda_{p_i}}(\mathbf{r}) = \sum_{j \mu \lambda} e^{i\pi(j_{p_i} - \lambda_{p_i} - 1)/2} (-1)^{1/2 + \sigma_{p_i}} Y_{j_{p_i} + \lambda_{p_i}}^{\mu_{p_i} - \sigma_{p_i}}(\theta, \phi)^* \Psi_{j_{p_i} \mu_{p_i} \lambda_{p_i}}(\mathbf{r}, \epsilon_{p_i}) e^{-i\delta_{j_{p_i} \lambda_{p_i}}(i)} \quad (3.2)$$

Equation 3.2 allows us to express the momentum vectors of the emitted conversion electrons in terms of  $\theta$  and  $\phi$  and use the formalism of spherical harmonics to describe the angular dependence and correlations between the emitted electrons.

In Equation 3.2,  $\delta_{j\lambda}$  are the electron wavefunction phase shifts for the free electron states. They are obtained from the electron wavefunctions in the asymptotic limit, as the radius goes to infinity. The continuum electron wavefunctions become:

$$\begin{aligned} u_{j\lambda}(r) &= \sqrt{\frac{W+1}{\pi p}} \cos[pr + \delta_{j\lambda} - (l+1)\pi/2] \\ v_{j\lambda}(r) &= -\sqrt{\frac{W-1}{\pi p}} \sin[pr + \delta_{j\lambda} - (l+1)\pi/2], \end{aligned}$$

where  $u(r)$  and  $v(r)$  are the radial solutions to the Dirac equation for unbound electrons in the potential created by the nucleus and orbital electrons [32].

We can now express the momentum directions of the emitted electrons in terms of  $\theta_i$  and

$\phi_i$ , giving the equation for  $dW_{ee}$  as

$$\begin{aligned}
 dW(\dots[q_i]^{n_i} \rightarrow \mathbf{p}_1\sigma_{p_1}\epsilon_{p_1}\mathbf{p}_2\sigma_{p_2}\epsilon_{p_2}) &= d\epsilon_{p_1}d\epsilon_{p_2}\delta(E_1 - E_2 - [\epsilon_{p_1} + \epsilon_{p_2} - \epsilon_{q_1} - \epsilon_{q_2}]) \\
 &\quad d\Omega_{p_1}d\Omega_{p_2}2\pi\frac{1}{2I_1+1}\sum_{M_1M_2}\sum_{\alpha_i}|\sum_{j_{p_1}j_{p_2}}\sum_{\mu_{p_1}\mu_{p_2}}\sum_{\lambda_{p_1}\lambda_{p_2}} \\
 &\quad e^{i\delta_{j_{p_1}\lambda_{p_1}}(1)}(-1)^{1/2+\sigma_{p_1}}C_{j_{p_1}+\lambda_{p_1}\mu_{p_1}-\sigma_{p_1}1/2\sigma_{p_1}}^{j_{p_1}\mu_{p_1}} \\
 &\quad Y_{j_{p_1}+\lambda_{p_1}}^{\mu_{p_1}-\sigma_{p_1}}(\theta_1, \phi_1)e^{-i\pi(j_{p_1}-\lambda_{p_1}-1)/2} \\
 &\quad e^{i\delta_{j_{p_2}\lambda_{p_2}}(2)}(-1)^{1/2+\sigma_{p_2}}C_{j_{p_2}+\lambda_{p_2}\mu_{p_2}-\sigma_{p_2}1/2\sigma_{p_2}}^{j_{p_2}\mu_{p_2}} \\
 &\quad Y_{j_{p_2}+\lambda_{p_2}}^{\mu_{p_2}-\sigma_{p_2}}(\theta_2, \phi_2)e^{-i\pi(j_{p_2}-\lambda_{p_2}-1)/2} \\
 &\quad H_{ee}([q_i]^{n_i} \rightarrow p_1p_2q_1q_2)|^2
 \end{aligned} \tag{3.3}$$

The  $C_{j_{p_1}+\lambda_{p_1}\mu_{p_1}-\sigma_{p_1}1/2\sigma_{p_1}}^{j_{p_1}\mu_{p_1}}$  terms are Clebsch-Gordon coefficients. Clebsch-Gordon coefficients describe the coupling of two angular momenta to make a total angular momentum in quantum mechanics. They are the expansion coefficients of the total angular momentum states in terms of the two uncoupled angular momentum states.

### 3.1.5 Interaction Hamiltonian

Let us denote  $H_{ee}([q_i]^{n_i} \rightarrow p_1p_2q_1q_2)$  as the matrix element for converting two electrons from electronic states  $|q_1\rangle$  and  $|q_2\rangle$  to final states  $|p_1\rangle$  and  $|p_2\rangle$  from an initial electron configuration of  $[q_i]^{n_i}$ .

The  $\hat{H}_{ee}(q_1q_2 \rightarrow p_1p_2; L)$  is the operator for the double internal conversion process. It mediates the conversion of two bound electrons from initial states  $|q_1\rangle$  and  $|q_2\rangle$  to final continuum states  $|p_1\rangle$  and  $|p_2\rangle$  by a nuclear transition of multipolarity  $L$ :

$$\begin{aligned}
 \hat{H}_{ee}(q_1q_2 \rightarrow p_1p_2; L) &= -\hat{a}_{p_2}^+\hat{a}_{p_1}^+\hat{a}_{p_1}\hat{a}_{p_2}C_{I_2M_2Lm}^{I_1M_1} \\
 &\quad \left\{ \sum_{L_1L_2}G_L(L_1\omega_1L_2\omega_2)\sum_{m_1m_2}C_{j_{q_1}\mu_{q_1}L_1m_1}^{j_{p_1}\mu_{p_1}}C_{j_{q_2}\mu_{q_2}L_2m_2}^{j_{p_2}\mu_{p_2}}C_{L_2m_2L_1m_1}^{Lm} \right. \\
 &\quad \left. -\sum_{L_1''L_2'}G_L(L_1''\omega_1''L_2'\omega_2')\sum_{m_1''m_2'}C_{j_{q_1}\mu_{q_1}L_1''m_1''}^{j_{p_2}\mu_{p_2}}C_{j_{q_2}\mu_{q_2}L_2'm_2'}^{j_{p_1}\mu_{p_1}}C_{L_2'm_2'L_1''m_1''}^{Lm} \right\},
 \end{aligned} \tag{3.4}$$

where  $\hat{a}_{q_i}$  are annihilation operators which serve to remove an electron from state  $|q_i\rangle$ . Conversely,  $\hat{a}_{p_i}^+$  are creation operators which serve to place an electron into state  $|p_i\rangle$ .

The double internal conversion operator mediates the sum of four processes which are illustrated in Figure 3.1[12]. The four processes are the four possible ways to convert two electrons in states  $|q_1\rangle$  and  $|q_2\rangle$  to final states  $|p_1\rangle$  and  $|p_2\rangle$ .

In Figure 3.1 and Equation 3.4  $\omega_1, \omega_2, \omega_1'', \omega_2'$  are the advanced potentials of the four different conversion pathways shown in Figure 3.1 and the corresponding multipolarities of the converting quanta are  $L_1, L_2, L_1'', L_2'$ . The possible values for the  $L$ 's are limited by the fact that  $L_1 + L_2 = L = L_1'' + L_2'$  and  $L$  is the total multipolarity of the single quantum transition with  $L = |I_1 - I_2|$ .

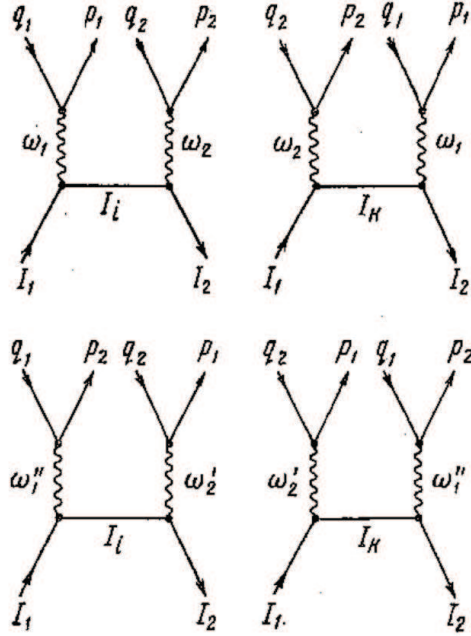


**Figure 3.1:** Feynman diagrams depicting the four possible pathways for double internal conversion.

The advanced potentials are defined as  $\omega_1 = \epsilon_{p_1} - \epsilon_{q_1}$ ,  $\omega_2 = \epsilon_{p_2} - \epsilon_{q_2}$ ,  $\omega_1'' = \epsilon_{p_2} - \epsilon_{q_1}$ ,  $\omega_2' = \epsilon_{p_1} - \epsilon_{q_2}$  where the  $\epsilon$ s denote the energies of the electronic states.

The possible reaction channels where  $L_1 + L_2 < L$  are physically possible but can be neglected compared with the contributions from the channels in which  $L_1 + L_2 = L$  [12].

The nuclear structure effects and conversion coefficients are bound up inside the  $G_L$  terms which consist of the sum of products of possible multipole combinations of electron conversion and nuclear transition.

Only two-quantum transitions competing with a magnetic transition are of interest in the present study, so only the  $G_L$  terms corresponding to magnetic transitions,  $G_{ML}$ , will be examined here. The different  $G_L$  terms corresponding to a two-quantum transition competing with an electric transition can be found in [12].

The  $G_L(L_1\omega_1L_2\omega_2)$  terms correspond to the upper two pathways represented in Figure 3.1, whereas the  $G_L(L_1''\omega_1''L_2'\omega_2')$  terms correspond to the lower two pathways:

$$\begin{aligned}
 G_{ML}(L_1\omega_1L_2\omega_2) = & [\delta_{L_10}\delta_{L_2L}\delta_{j_{p_1}j_{q_1}}\sqrt{4\pi}\langle p_1[E0\omega_1]q_1\rangle\langle p_2[ML\omega_2]q_2\rangle\langle I_2||(E0\omega_1ML\omega_2)||I_1\rangle \\
 & +\delta_{L_1L}\delta_{L_20}\delta_{j_{p_2}j_{q_2}}\sqrt{4\pi}\langle p_1[ML\omega_1]q_1\rangle\langle p_2[E0\omega_2]q_2\rangle\langle I_2||(ML\omega_1E0\omega_2)||I_1\rangle \\
 & +4\pi\langle p_1[ML_1\omega_1]q_1\rangle\langle p_2[EL_2\omega_2]q_2\rangle\langle I_2||(ML_1\omega_1EL_2\omega_2)L||I_1\rangle \\
 & +4\pi\langle p_1[EL_1\omega_1]q_1\rangle\langle p_2[ML_2\omega_2]q_2\rangle\langle I_2||(EL_1\omega_1ML_2\omega_2)L||I_1\rangle]
 \end{aligned} \quad (3.5)$$

$$\begin{aligned}
G_{ML}(L_1''\omega_1''L_2'\omega_2') = & [\delta_{L_1''0}\delta_{L_2'L}\delta_{j_{p_2}j_{q_1}}\sqrt{4\pi}\langle p_2[E0\omega_1'']q_1\rangle\langle p_1[ML\omega_2']q_2\rangle\langle I_2||(E0\omega_1''ML\omega_2')||I_1\rangle \\
& + \delta_{L_1''L}\delta_{L_2'0}\delta_{j_{p_2}j_{q_2}}\sqrt{4\pi}\langle p_2[ML\omega_1'']q_1\rangle\langle p_2[E0\omega_2']q_2\rangle\langle I_2||(ML\omega_1''E0\omega_2')||I_1\rangle \\
& + 4\pi\langle p_2[ML_1''\omega_1'']q_1\rangle\langle p_1[EL_2'\omega_2']q_2\rangle\langle I_2||(ML_1''\omega_1''EL_2'\omega_2')L||I_1\rangle \\
& + 4\pi\langle p_2[EL_1''\omega_1'']q_1\rangle\langle p_1[ML_2'\omega_2']q_2\rangle\langle I_2||(EL_1''\omega_1''ML_2'\omega_2')L||I_1\rangle]
\end{aligned} \quad (3.6)$$

### 3.1.6 Reduced Two Quantum Transition Matrices

The  $\langle I_2||(L_1\omega_1L_2\omega_2)L||I_1\rangle$  terms are the reduced matrix elements of the two quantum nuclear  $\gamma\gamma$  transition, which are described in [10]. These reduced matrix elements represent the nuclear component of the two quantum transition and are defined below:

$$\begin{aligned}
\langle I_2||(S_1L_1\omega_1S_2L_2\omega_2)L||I_1\rangle = & \left\{ \sum_k u(I_2I_1L_2L_1; LI_k) \frac{\langle I_2||S_2L_2||I_k\rangle\langle I_k||S_1L_1||I_1\rangle}{E_k - E_2 - \omega_2} \right. \\
& \left. + \sum_n u(I_2I_1L_1L_2; LI_n) \frac{\langle I_2||S_1L_1||I_n\rangle\langle I_n||S_2L_2||I_1\rangle}{E_n - E_2 - \omega_1} \right\} 3.7
\end{aligned}$$

Here  $S_1$  and  $S_2$  represent the character of the two transitions, whether they are magnetic or electric transitions. The sums are taken over all the possible real excited states of the nucleus, represented by  $I_k$  and  $I_n$ , which can be coupled to the initial and final state by virtual electromagnetic transitions of multipole order and character  $S_iL_i$ .

An equivalent definition can be found in [4].

The reduced matrix elements  $\langle I_i||SL||I_k\rangle$  are described in [10] and are described below where  $\mathbf{Y}_{LM}^\Lambda$  are vector spherical harmonics [33].

$$\langle j_n||ML||j_k\rangle C_{j_n\mu_n LM}^{j_k\mu_k} = \langle j_n\mu_n|\sqrt{4\pi}(\frac{r_i}{R_0})^{L-1}\mathbf{Y}_{LM}^{-1*}[\mathbf{l}_i\delta_i + \frac{1}{2}(L+1)\mu_i\hat{\sigma}_i]|j_k\mu_k\rangle \quad (3.8)$$

$$\langle j_n||EL||j_k\rangle C_{j_n\mu_n LM}^{j_k\mu_k} = \langle j_n\mu_n|\sqrt{4\pi}(\frac{r}{R_0})^L\mathbf{Y}_{LM}^*(\mathbf{r})|j_k\mu_k\rangle \quad (3.9)$$

The  $u(abcd; ef)$  terms in Equation 3.7 are the normalised Racah coefficients. They are coupling constants that describe the relationship between three different angular momentum vectors. They are related to the normal Racah coefficients  $W(abcd; ef)$  by the following relationship:

$$u(abcd; ef) = \sqrt{2e+1}\sqrt{2f+1}W(abcd; ef).$$

### 3.1.7 Partial Internal Conversion Coefficients

The brackets  $\langle p[EL\omega]q\rangle$  and  $\langle p[ML\omega]q\rangle$  signify the electronic component of the two-quantum transition. They denote the reduced integrals for the conversion of an electron from the  $q$ th subshell, a state defined by  $\epsilon_q, j_q, \lambda_q$ , into a continuum state  $|p\rangle$  defined by

$\epsilon_p, j_p, \lambda_p$ , caused by a nuclear  $L$ -multipole of energy  $\omega$ . They are defined:

$$\begin{aligned}\langle p[EL\omega]q \rangle &= \alpha_L(qp\omega) \frac{e}{2\pi} \frac{\omega^{L+\frac{1}{2}} R_0^L}{(2L+1)!!} \sqrt{\frac{L+1}{L}} \sqrt{\frac{2L+1}{2j_q+1}} \\ \langle p[ML\omega]q \rangle &= \beta_L(qp\omega) \frac{e}{2\pi M R_0} \frac{\omega^{L+\frac{1}{2}} R_0^L}{(2L+1)!!} \sqrt{\frac{2L+1}{L+1}} \sqrt{\frac{2L+1}{2j_q+1}}\end{aligned}\quad (3.10)$$

The  $\alpha_L(qp\omega)$  and  $\beta_L(qp\omega)$  terms are the partial internal conversion coefficients for electrons in state  $|q\rangle$  being placed into state  $|p\rangle$  by a nuclear  $L$ -multipole of electric or magnetic character, respectively.

The internal conversion coefficient,  $\alpha(K_i, \pi L)$  from a particular initial electron state, defined by  $K$  or  $j, \lambda$ , of a particular nuclear transition of character  $\pi$  and multipolarity  $L$  is

$$\alpha(K_i, \omega\pi L) = \sum_K |M_{KK_i}(\omega\pi L)|^2 \quad (3.11)$$

It is these  $M_{KK_i}(\pi L)$ s which are the partial conversion coefficients used in equations 3.10. The mod square of these partial internal conversion coefficients give the probability of an electron being internally converted from state  $K_i$  to state  $K$  by a nuclear transition of energy  $\omega$ , parity or character  $\pi$ , and multipolarity,  $L$  [32].

### 3.1.8 Selection Rules for Conversion Electrons

A nuclear transition of  $L$ -multipole order can only place an electron into a particular state depending on the multipolarity of the transition and whether the transition is electric or magnetic in nature.

An  $EL$  electric transition of multipolarity  $L$  can only place a K shell electron, an electron in the  $1s_{1/2}$  state, ( $j = \frac{1}{2}, \lambda = \frac{-1}{2}$ ) or  $K = -1$  into states of Dirac quantum number  $K = L, -(L+1)$ . On the other hand, an  $ML$  magnetic transition of multipolarity  $L$  can place a K shell electron into states of Dirac quantum number  $K = -L, (L+1)$ .

Electric and magnetic transitions have opposite parity of the same multipolarity. Dirac states with the same  $|K|$  have the same total angular momentum but the electron states with negative values for  $K$ , have  $\lambda = -\frac{1}{2}$  and opposite parity compared to those states with positive values for  $K$  which have  $\lambda = \frac{1}{2}$ .

### 3.1.9 Angular Separation Function

The probability of emission of two electrons depends on the separation angle between the two particles, but not on their absolute angles. We can then define our quantisation axis to be that of the direction of emission of electron state  $|p_1\rangle$ . This effectively sets  $\mathbf{p}_1 = \hat{z}$  or  $(\theta_1, \phi_1) = (0, 0)$  and  $\theta_2$  is transformed to  $\theta_{12}$  or the separation angle between the two emitted electrons [34, 35].

We can then integrate over the solid angle of the first electron,  $d\Omega_1 = \sin(\theta_1)d\theta_1d\phi_1$  and the azimuthal angle of the second electron,  $d\phi_2$ . This gives us the angular correlation

function which depends only on the energy of one of the electrons and on the separation angle between the two particles. The final probability function also includes a sum of the spin projections of the emitted electrons. This gives:

$$dW(e_1, \theta_{12}) = 8\pi^2 dW(\epsilon_1 = e_1, \epsilon_2 = E - e_1, \theta_1 = 0, \phi_1 = 0, \theta_{12}, \phi_2 = 0) \quad (3.12)$$

## 3.2 Program Development

Over the course of the work, I have developed a program, `DoubleInternalConversionKShell`, which calculates the transition rate for the double internal conversion process of K shell electrons in a nuclear decay. This program solves the equations outlined in the previous section, following the theoretical model produced by Grechukhin [12].

The program takes as input parameters the energy of one of the electrons, the separation angle between the two emitted electrons, the proton and neutron numbers of the nucleus in question, the multipolarity and energy of the transition, and the reduced  $\gamma\gamma$  transition matrix elements.

The program returns the transition rate of the double internal conversion process of K-shell electrons in units of  $[m_e c^2]^{-1} rad^{-1} s^{-1}$  for a particular given electron energy and separation angle.

The program solves Equations 3.12, 3.3, 3.4, 3.5, 3.6, and 3.10. The partial internal conversion coefficients,  $\alpha_L(q\omega)$  and  $\beta_L(q\omega)$ , referenced in Equation 3.10, and the electron phase shifts,  $\delta_{j\lambda}$ , referenced in Equation 3.3, are calculated by calling the CATAR program [32] modified for use in this work by Andrew Stuchbery.

The CATAR program works by numerically solving the Dirac equation for bound and continuum electrons in the presence of a finite-sized charged nucleus. The radial components  $u_K$  and  $v_K$  of the Dirac spinor, which describes the electron, are the solutions to the coupled differential equations

$$\frac{du_K}{dr} = -\left(\frac{K}{r}\right)u_K + [W + 1 - V(r)]v_K \quad (3.13)$$

$$\frac{dv_K}{dr} = \left(\frac{K}{r}\right)v_K - [W - 1 - V(r)]u_K \quad (3.14)$$

where  $V(r)$  is the electrostatic potential of the finite nucleus which is treated as a uniformly charged liquid drop and  $W$  the energy of the electron. The effect of atomic screening on the effective potential is taken into account through the use of the relativistic Hartee-Fock-Slater screening function or the Gaspar screening function [32]. Once the electron wavefunctions are determined, all necessary values and properties can then be calculated such as the partial internal conversion coefficients and the electron phase shifts.

The program writes the appropriate input file for the CATAR program for the particular nuclear transition and ejected electron energy and reads the CATAR output file to obtain the partial conversion coefficients and electron phase shifts.

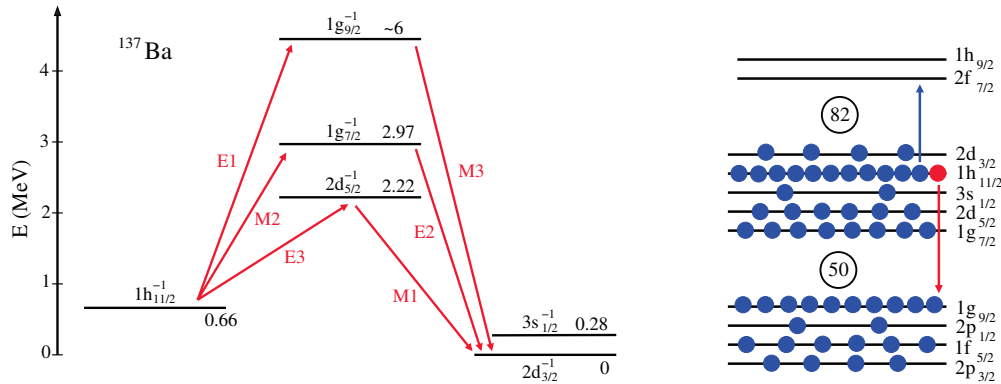


**Figure 3.2:** Possible decay paths of the two-photon decay from the  $1h_{11/2^-}$  neutron hole state to the  $2d_{3/2+}$  ground state through intermediate neutron hole states (left-hand side). On the right hand side the neutron configuration in the independent particle model of the  $1h_{11/2^-}$  state is shown. A transition through the  $1g_{9/2^+}$  state is allowed (red arrow). On the other hand an excitation from a neutron to the  $2f_{7/2^+}$ -state is not possible (blue arrow), since there is no one-step de-excitation back to the  $2d_{3/2+}$  ground state. [5].

The program takes around 20 seconds to calculate a transition rate for a given energy value and separation angle.

In order to produce the double differential cross section with respect to electron energy and separation angle, a matrix of transition rates for a range of energy and separation angles is calculated. A smooth distribution is then obtained via the use of a surface spline fitting function.

The program has been used to do the first comprehensive calculations on double internal conversion. The double differential cross section for the ejection of two K-shell electrons in the 662 keV transition in  $^{137}\text{Ba}$  has been calculated describing for the first time the energy distribution and angular dependance of the two emitted electrons. These calculations are covered in more detail in Sections 3.3, 3.4.

### 3.3 Application to $^{137m}\text{Ba}$

This work focuses on the 662 keV M4 transition in  $^{137}\text{Ba}$  from an excited  $\frac{11}{2}^-$  state to the  $\frac{3}{2}^+$  ground state and possible two-quantum processes.

The 662 keV transition can proceed by eight possible two quantum pathways for the double internal conversion process where  $L_1 + L_2 = L = 4$ . They are the E0M4, E1M3, E2M2, E3M1, M1E3, M2E2, M3E1, M4E0 pathways. Some of these pathways can be explained by the movement of the odd neutron hole state in the  $^{137}\text{Ba}$  nucleus. This pathways can be seen in Figure 3.2.

The E0M4 and M4E0 pathways are not considered in this work due to the lack of calculated E0M4 and M4E0 reduced transition matrix elements. However, the  $E0$  matrix element is expected to be small and should not have a significant impact of the process.

Each two-quantum pathway proceeds via a set of intermediate excited states of  $^{137}\text{Ba}$  each

$S_1 L_1 S_2 L_2$	Intermediate state spin/parity
$E1M3$	$9/2^+$
$E2M2$	$7/2^-$
$E3M1$	$5/2^+$
$M1E3$	$9/2^-$
$M2E2$	$7/2^+$
$M3E1$	$5/2^-$

**Table 3.1:** Table of the spin and parity assignment of the intermediate nuclear states accessed by each two quantum pathway

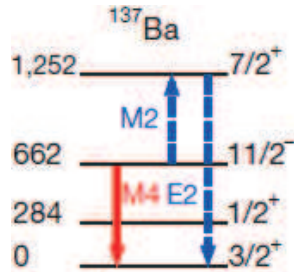


**Figure 3.3:** Figure showing the lowest lying excited state of  $^{137}\text{Ba}$  above the 662 keV state. It is a valid intermediate state in the  $M2E2$  decay pathway [4].

with the appropriate spin and parity for each pathway, depending on the multipolarity and parity of the transitions involved. The spins and parities of the intermediate nuclear states for each pathway have been tabulated in Table 3.1.

The contributions to the reduced  $\gamma\gamma$  transition matrix elements by each excited intermediate state are inversely weighted according to the excitation energy of each intermediate state as shown in Equation 3.7 [10, 4].

This suggests that the two quantum decay process should proceed more strongly through pathways which have relatively low lying states such as the  $M2E2$  reaction channel which passes through the 1.252 MeV  $7/2^+$  state as shown in Figure 3.3.

Recent work on double gamma decay in  $^{137}\text{Ba}$  has been done by Christopher Walz in 2015 [4]. The reduced  $\gamma\gamma$  transition matrix elements for the six reaction channels showcased in Table 3.1 have been calculated using the quasiparticle phonon model. The elements calculated by Walz are not the full reduced  $\gamma\gamma$  transition matrix elements showcased in Equation 3.7 but are instead solely the nuclear component of a particular multipole combination; the effect of the angular momentum coupling can be included later. The definition of what was calculated is shown in Equation 3.15 below.

$$\alpha_{S'L'SL} = \sum_n \frac{\langle I_f || i^{L'-S'} M(S'L') || I_n \rangle \langle I_n || i^{L-S} M(SL) || I_i \rangle}{E_n - 0.5E_0} \quad (3.15)$$

The quasiparticle-phonon model treats the nucleus as a set of coupled fermions to form bosonic states. The behaviour of these pairs, their excitations and the splitting of these pairs can then be used to describe the nuclear states. Any detailed analysis of the quasi-

$S_1 L_1 S_2 L_2$	Matrix Element ( $e^2 \text{fm}^4 \text{MeV}^{-1}$ )
$E1M3$	-2.63
$E2M2$	-2.52
$E3M1$	9.47
$M1E3$	-0.58
$M2E2$	42.60
$M3E1$	0.28

**Table 3.2:** Table of the transition strengths of each multipole combination [4].

particle phonon model will not be undertaken in this work. For more information on the quasiparticle model, see [36].

The transition elements calculated by Walz have been calculated by removing the energy dependence of the transition quanta and instead taking the average energy of the quanta, half the transition energy. This does not have a significant effect on the values for the matrix values except for contributions by the low lying excited states. There is an estimated 10% error in the values of the matrix elements [4]. They are tabulated in Table 3.2.

Different standard conventions are used by Grechukhin [10] and Walz [4] with respect to the symmetry relations of the multipole transition operators. In the work by Grechukhin [10], the multipole operators are invariant under the combined set of operations,  $R_y PI$  which correspond to rotation about the  $y$  axis by  $\pi$ , parity inversion, and time reversal. Walz [4] however was used the  $R_y I$  convention, where the multipole operator is invariant under the combined rotation and time reversal operation. In order then to obtain real matrix elements and match the symmetry behaviour of the nuclear states, the reduced transition matrix elements include an  $i^{L-S}$  factor in the definition used by Walz. More information on the different symmetry conventions for transition operators and nuclear states can be found in [1].

It was assumed that in the model of Grechukhin [12] the transition channels with  $L_1 + L_2 > L$  have an insignificant effect on the overall process. The  $L=5$  matrix elements calculated by Walz corroborate this assumption [4].

As noted above, the partial internal conversion coefficients,  $\alpha_L(q\omega)$  and  $\beta_L(q\omega)$  and the electron phases,  $\delta_{j,\lambda}$  were calculated using the CATAR program.[32]

As outlined in Section 3.1.8, only certain electronic states can be filled by the set of possible  $L = 4$  transition combinations. These possible states, represented in by the Dirac quantum number,  $(j, \lambda)$  notation, and spectroscopic notation  $l_j$ , and the possible converting transitions are tabulated in Table 3.3.

### 3.4 Theoretical Predictions of Double Internal Conversion in $^{137m}\text{Ba}$

The model was used to characterise the 662 keV M4 transition of the  $^{137m}\text{Ba}$  isomer with respect to double internal conversion. The double differential cross section is the probability of emission of a pair of electrons, one with energy  $\epsilon_1$ , the other with the complementary energy and a certain separation angle,  $\theta_{sep}$  between them. This cross

$K$	$(j, \lambda)$	$l_j$	$SL$
-1	$1/2, -1/2$	$s_{1/2}$	$M1$
1	$1/2, 1/2$	$p_{1/2}$	$E1$
-2	$3/2, -1/2$	$p_{3/2}$	$E1, M2$
2	$3/2, 1/2$	$d_{3/2}$	$E2, M1$
-3	$5/2, -1/2$	$d_{5/2}$	$E2, M3$
3	$5/2, 1/2$	$f_{5/2}$	$E3, M2$
-4	$7/2, -1/2$	$f_{7/2}$	$E3$
4	$7/2, 1/2$	$g_{7/2}$	$M3$

**Table 3.3:** Table of the various electron states accessed by different electromagnetic transitions.

section has been calculated using equation 3.12 for each of the three multipole combinations ( $E1M3 + M3E1$ ,  $E2M2+M2E2$ ,  $E3M1 + M1E3$ ) and are shown in Figures 3.4, 3.5, and 3.6.

The y-axis of the Figures 3.4, 3.5, and 3.6 in are degrees with the x-axis in MeV. The colour axis represents the probability of emission in  $[m_e c^2]^{-1} \text{ rad}^{-1} s^{-1}$ .

The three component combinations show strong differences in the distributions of emission probability with respect to energy sharing and the angular separation between emitted electrons. The  $E2M2 + M2E2$  process strongly prefers equal energy sharing between electron and emission with large emission angles, clearly visible in Figure 3.5. In comparison, the  $E1M3 + M3E1$  process prefers unequal energy sharing but with large separation angle and the  $E3M1 + M1E3$  process selects for extremely unequal energy sharing.

The double differential cross section for the total process is not the sum of the contributions from these combinations as there are interference effects between the possible reaction channels. The total double differential cross section has been calculated and is shown in Figure 3.7.

The double differential cross section of the total double internal process is mostly similar in form to the  $E2M2 + M2E2$  process. This is expected as the matrix element for the  $M2E2$  pathway is the largest, larger than the next largest, the  $E3M1$  pathway, by 4 times as shown in Table 3.2. Ignoring electronic effects, the weight of each process scales by the square of the matrix element, suggesting the  $M2E2$  will dominate by around at least a factor of 10 times. The total distribution is however more spread than that of the  $E2M2 + M2E2$  process and has a lower peak. It does however peak strongly in the region of equal energy sharing and large separation angle.

The total rate of double internal conversion of the K shell in the 662 keV transition of  $^{137m}\text{Ba}$  has been calculated by integrating the obtained total double differential cross section and the theoretical estimate is

$$P_{KK} = 4.99 \times 10^{-10} \text{ s}^{-1}$$

The K electron single conversion decay rate is

$$P_K = 3.80 \times 10^{-4} \text{ s}^{-1}$$

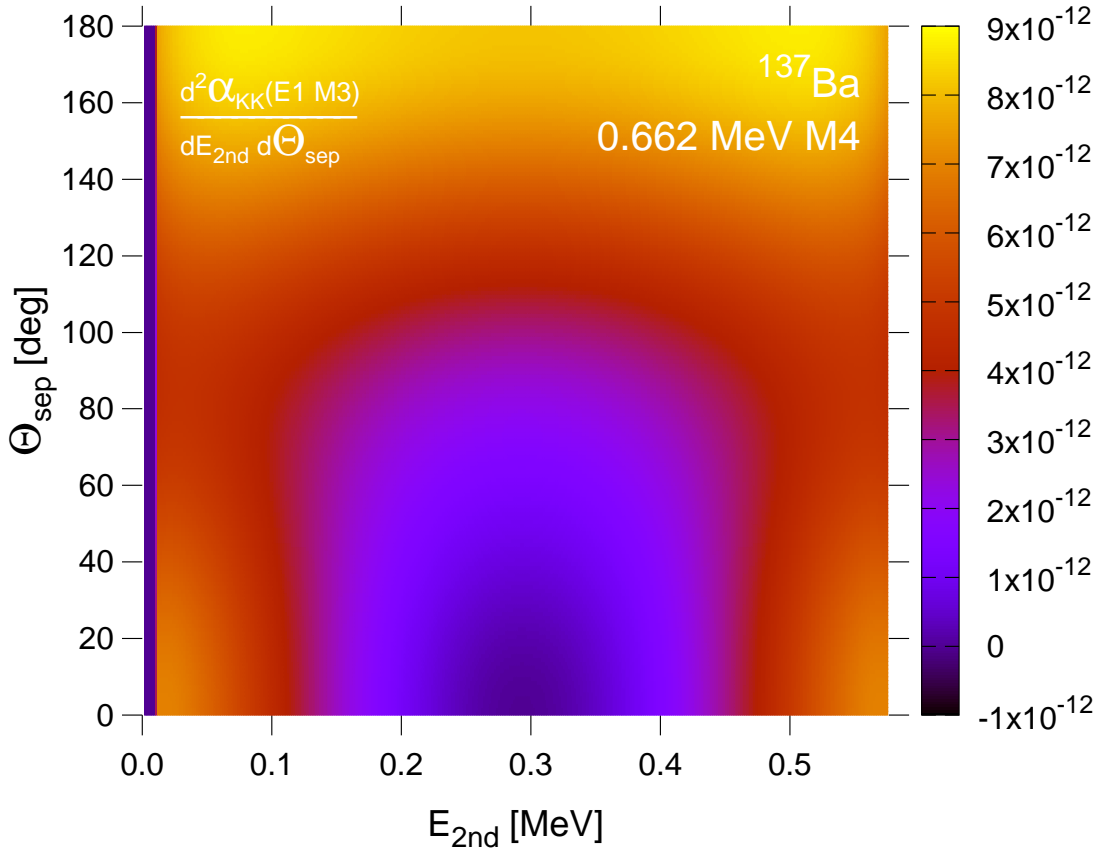


**Figure 3.4:** The double differential cross section of the E1M3+M3E1 two quantum process.

This gives a relative rate of

$$\frac{P_{KK}}{P_K} = 1.32 \times 10^{-6}$$

This is a very similar ratio to the other investigated two quantum decay process in  $^{137m}\text{Ba}$ , the rate of the double gamma process relative to the single gamma decay, which was found by Walz to be  $P_{\gamma\gamma}/P_\gamma = 2.06(37) \times 10^{-6}$ .

### 3.5 Comparison to Alternative KK Processes

As discussed in Section 2.2, the dominant alternative double K-shell ejection process in  $^{137m}\text{Ba}$  is the shake off process [3, 15]. The double differential cross section of the shake off process with respect to the separation angle between the K conversion electron and a K-shell shake off electron and shake off electron energy has never been calculated in the literature. However, the theoretical energy spectrum of K-shell shake off electron accompanying K-shell internal conversion has been calculated by Mukoyamma [15]. This spectrum is plotted in Figure 3.8. The solid line depicts the distribution of interest which is the relativistic one step theory. The dashed line is an older theoretical estimate which

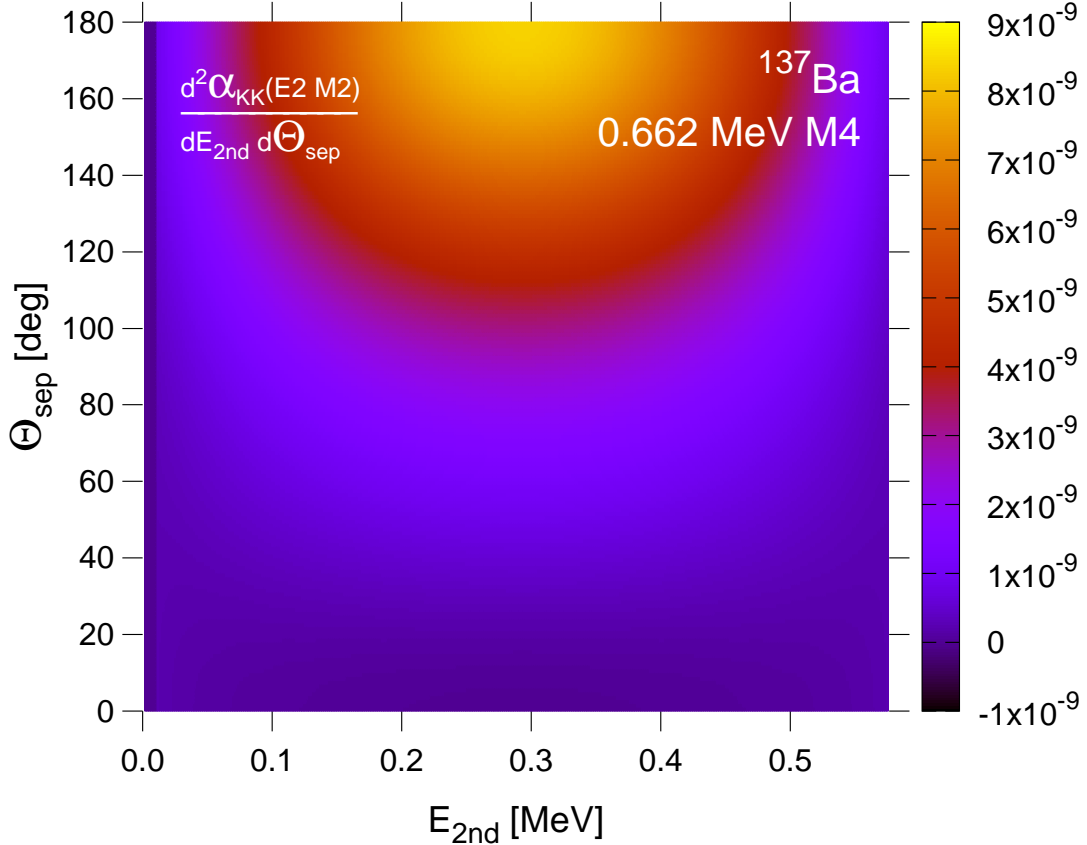


**Figure 3.5:** The double differential cross section of the E2M2+M2E2 two quantum process.

does not conserve energy and is defunct and the double dashed line is a non-relativistic theory.

The total double internal conversion process of K shell electrons in  $^{137m}\text{Ba}$  has been calculated using the program described in Section 3.2. This energy spectrum is plotted in Figure 3.9.

The shake off electron energy spectrum is strongly weighted towards the emission of a low energy shake off electron. The probability of the emission of a shake off electron falls to around  $3 \times 10^{-7}$  at equal energy sharing, the emission of the shake off electron at 293 keV. This is seen in Figure 3.8. Conversely, the probability of emission of double internally converted electrons peaks at equal energy sharing at 293 keV at a value around  $2 \times 10^{-6}$ .

This suggests that an experiment that preferentially selects electrons of equal energy, each at an energy around 293 keV, will strongly select for electrons emitted from the double conversion process as opposed to those electrons emitted by shake off. It is precisely this kind of experiment that has been conducted here at the ANU in this work using the Superconducting Electron Spectrometer (Super-e). The rest of this work will discuss the experimental apparatus, procedure, and results, especially in comparison with the theoretical predictions.

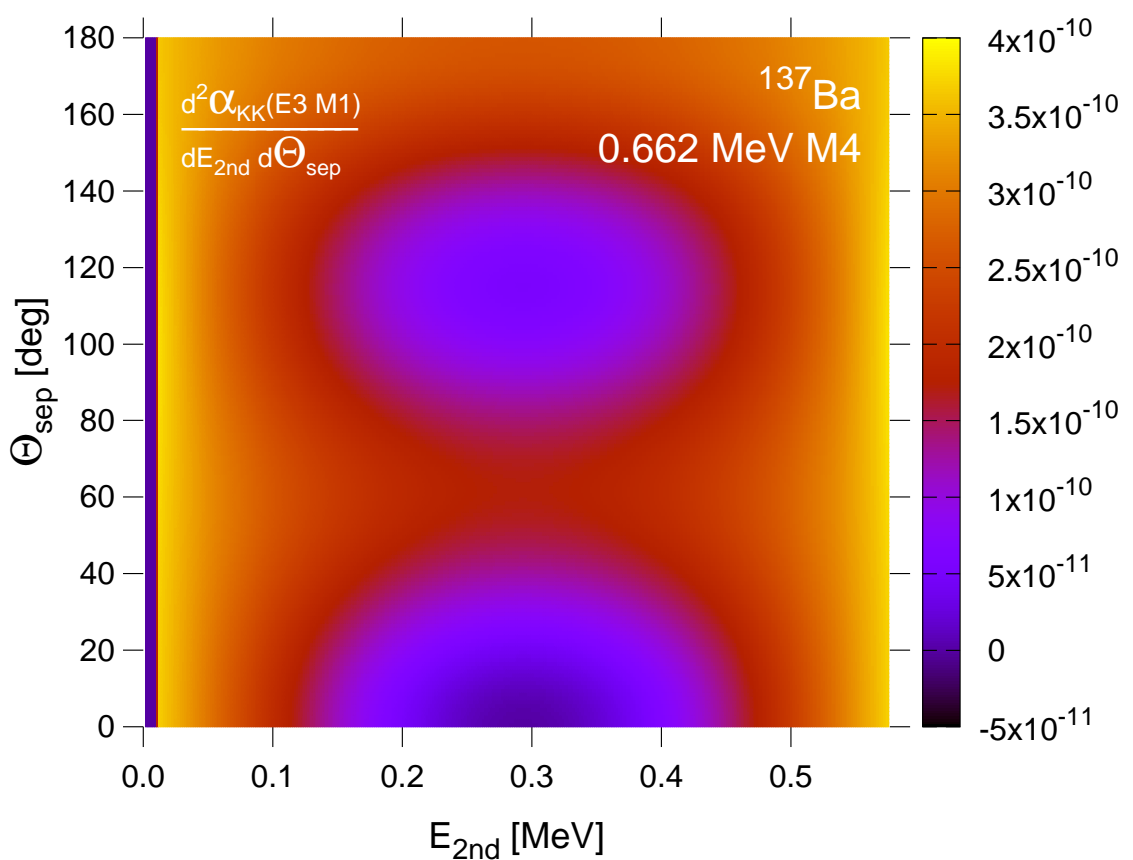


**Figure 3.6:** The double differential cross section of the E3M1+M1E3 two quantum process.

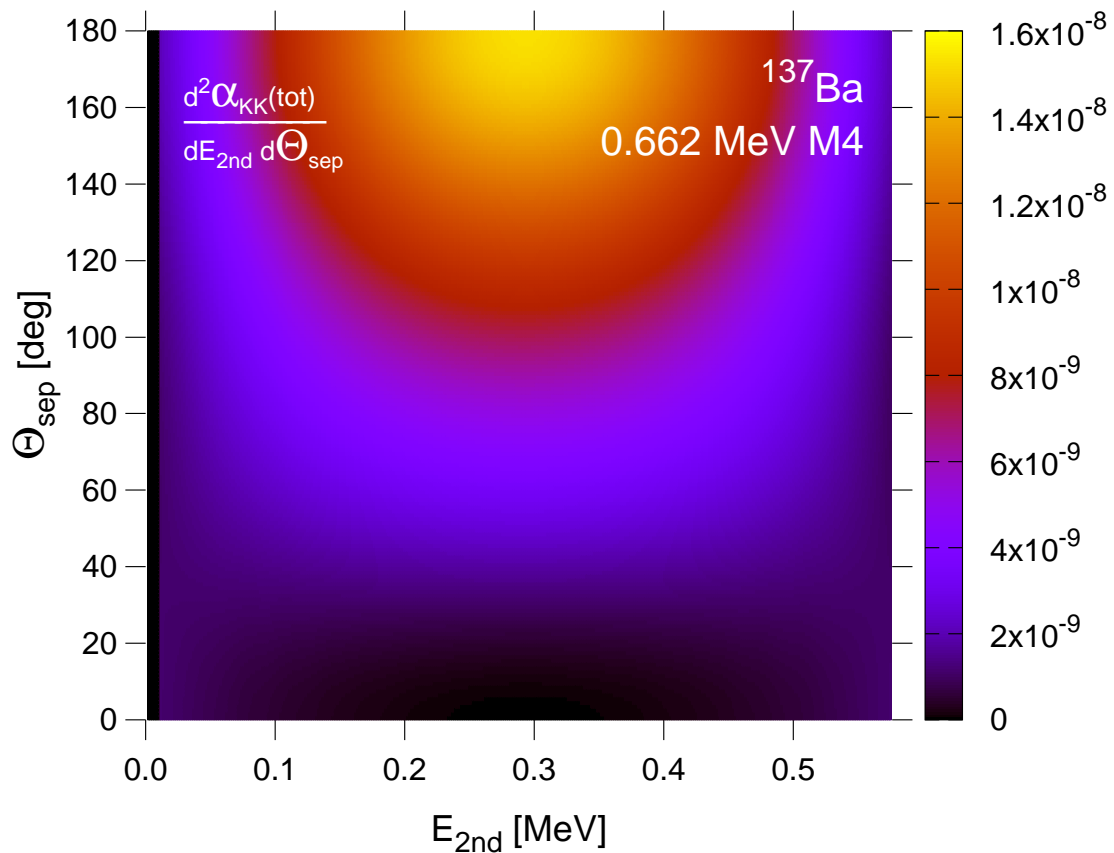


**Figure 3.7:** Double differential cross section with respect to separation angle an electron energy for the total double internal conversion process in the decay of  $^{137m}\text{Ba}$

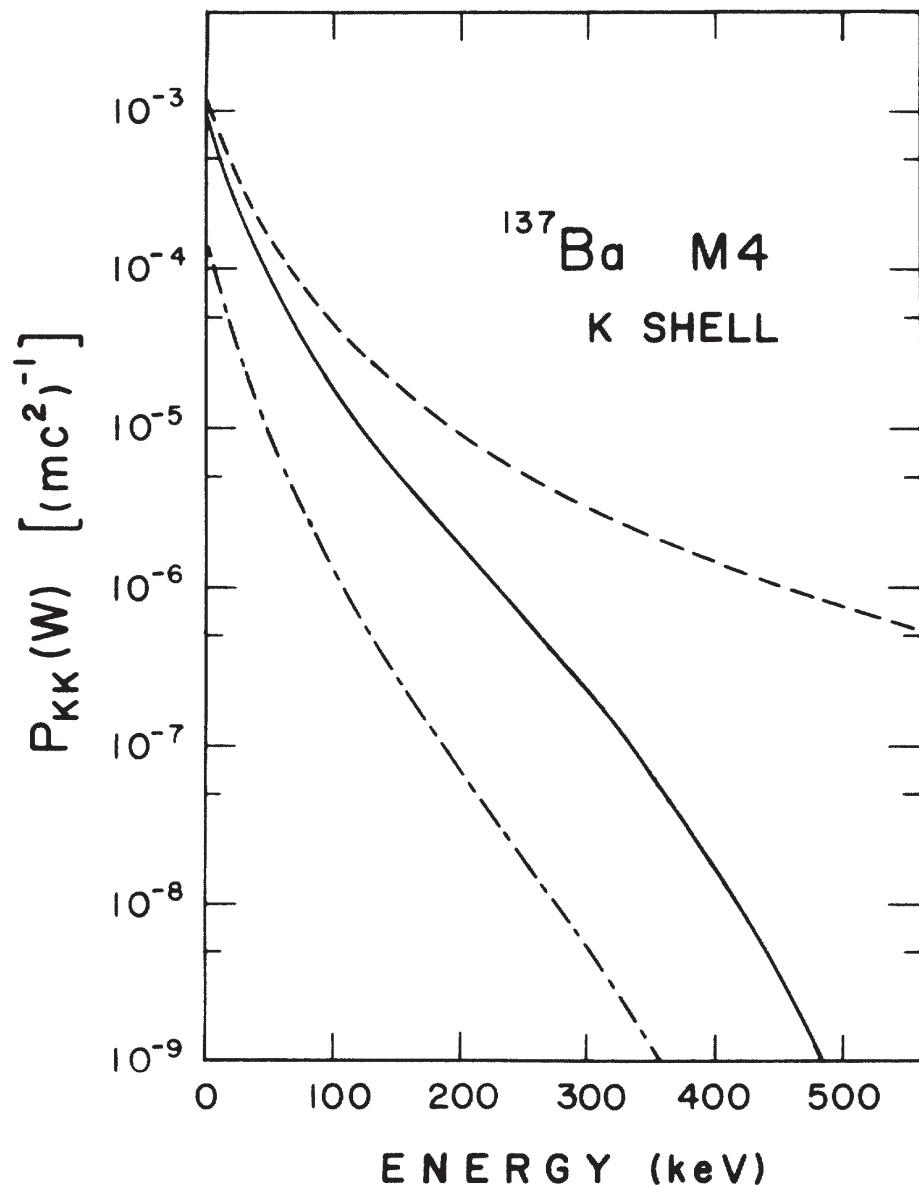


**Figure 3.8:** Plot of expected energy spectrum of K shake off electrons accompanying K conversion electron from  $^{137}\text{Ba}$  [15]

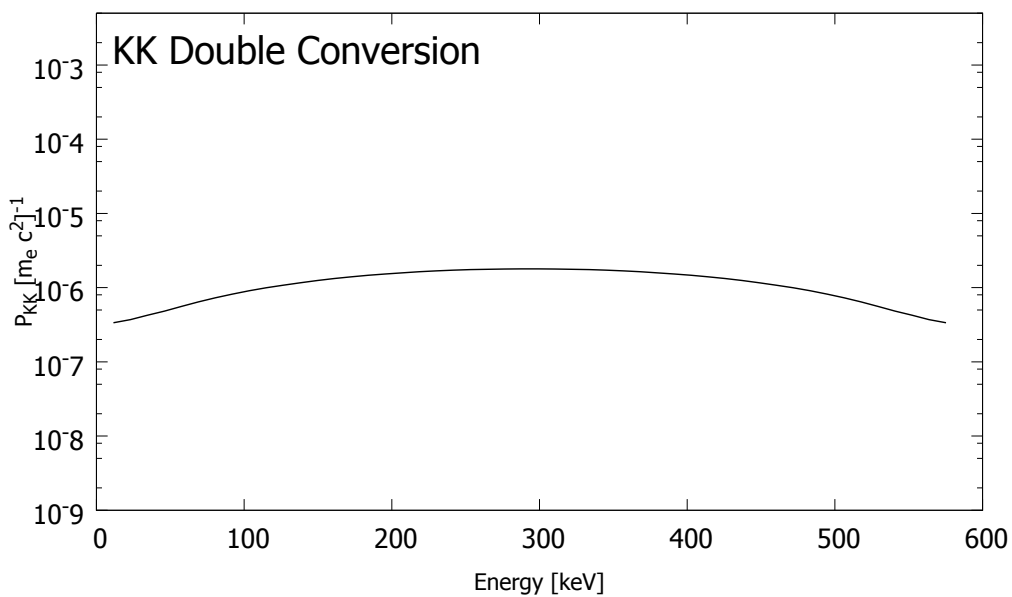


**Figure 3.9:** Plot of theoretical KK double internal conversion energy spectrum for the 662 keV M4 transition of  $^{137}\text{Ba}$

# Experimental Apparatus

The superconducting electron spectrometer or Super-e is a magnetic lens spectrometer designed by Tibor Kibédi for electron and electron/positron pair spectroscopy. The spectrometer works through the use of a magnetic field and envelope-baffle system to select a narrow momentum band of charged particles of interest, electrons or positrons, from the reaction background. [37]

## 4.1 Spectrometer design

The Super-e consists of a superconducting solenoid, two central lead baffles, a diaphragm, and an array of six SiLi detectors.

The superconducting solenoid is used to produce a strong axial magnetic field essential for the momentum selection. The superconducting solenoid consists of 3 sets of coils: short end, target, and long end coils. The solenoid is submerged within a liquid helium reservoir which is surrounded by a liquid nitrogen precooling jacket.

The three coils produce a relatively uniform axial magnetic field directed along the central bore of the super-e with an inhomogeneity of -3.7 to 1.6% [37]. A maximum current of 50 Amp produces a maximal magnetic field of 2.03 Tesla at the target position on the central axis.

There are two central baffles and a diaphragm in the bore of the Super-e. The two torpedo shaped central baffles are made of HeavyMet, a dense tungsten alloy, to stop direct radiation such as gamma-rays from reaching the detectors; they are part of energy

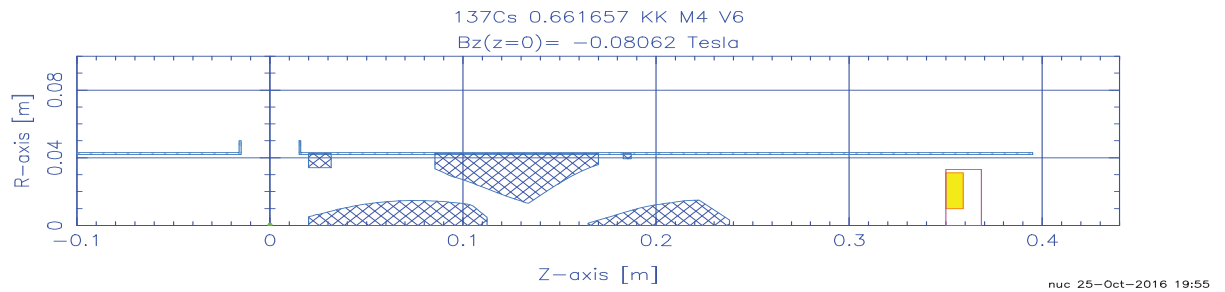


**Figure 4.1:** Radial cross section of the Super-e. The baffles are shown in crosshatching, the source position is the green dot at the origin of the axes, the Miel detector array is represented in pink with the active detector segments displayed in yellow

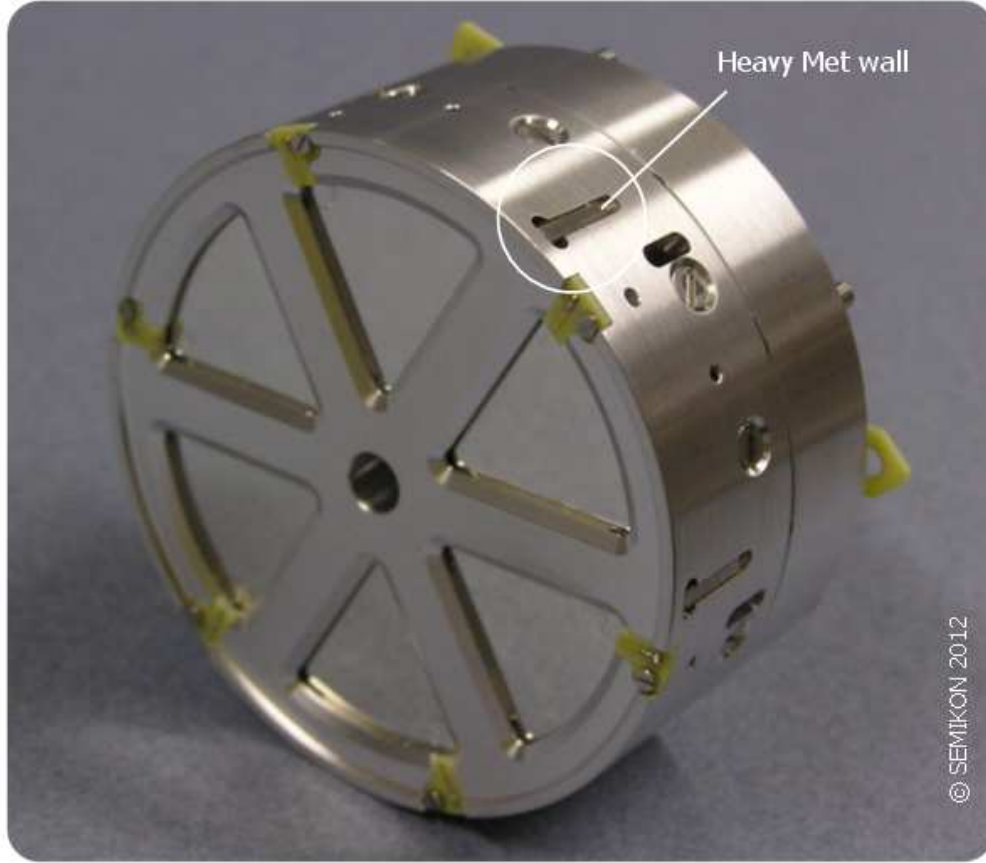


**Figure 4.2:** Picture of the Miel detector array. The HeavyMet strips are labelled and the six detectors are visible between the separating dividers.

selection mechanism. The two central baffles and the diaphragm serve to define a set of trajectories that charged particles must follow in order to be detected. Otherwise, they will strike the baffles or walls and not reach the detectors. The geometry of the baffles and detectors is visible in Figure 4.1.

The detector system is the Miel detector array. It consists of 6 SiLi detectors to detect electron-electron or electron-positron coincidence events. The energy resolution of the detectors is 2.5 keV full width at half maximum. The detectors are placed in a circular arrangement with each detector face making up a sector of the circle. The sectors/detectors are separated from each other by HeavyMet strips. These strips prevent the scattering of the incident electrons from one crystal to another and so prevent cross-talk events whereby one electron could scatter out of one detector into a neighbouring detector. The Miel detector is visible in Figure 4.2

In addition to the SiLi detectors, a Compton suppressed gamma ray detector, named Apterix, is placed on a radial direction from the target/source positron.

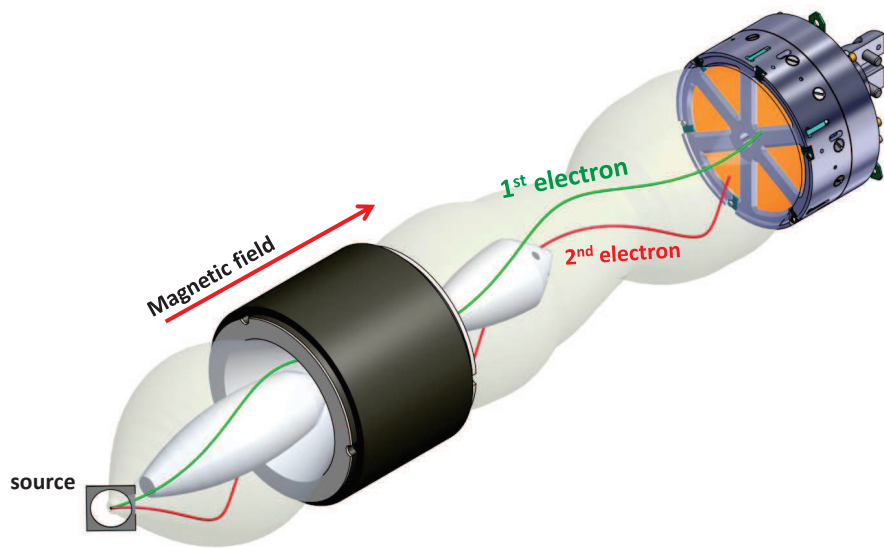


**Figure 4.3:** Illustration of the behaviour of charged particles inside the Super-e. The two electrons are transported by the magnetic field to the detector past the baffle system.

## 4.2 Magnetic selection

Charged particles moving inside a magnetic field experience a force at right angles to both the direction of motion of the particle and the direction of the magnetic field. This means charged particles in a uniform magnetic field will move in a helical fashion. The radius of the helix in the Super-e depends on both the energy of the charged particle and also the emission angle from the source. Only particles of appropriate energy and emission angles will be able to navigate past the baffles to reach the detector. Those of inappropriate energy or emission angle will strike the walls or baffles and not make it to the detectors. An illustration of the behaviour of charged particles inside the Super-e is given in Figure 4.3.

The combination of geometrical constraints and set magnetic field strength defines an acceptance window with regard to energy of the emitted particles, summing over the range of emission angles.

As noted above, the probability of a particular particle reaching the detectors depends on the energy and takeoff angles of the particle. Therefore it is necessary to know the double differential cross section - the probability of emission with respect to the energy and angle of the particle, or angles in the case of double conversion electron emission, to characterise the response of the Super-e to a particular transition and so determine the appropriate efficiency of the Super-e in a particular measurement.

Clearly, without the efficiency of the Super-e for a process, it is not possible to understand the results in a quantitatively meaningful way.

### 4.3 Super-e efficiency

The absolute efficiency of the Super-e to various processes is essential to understanding the experimental results. In that regard, the efficiency of the Super-e with respect to K-shell internal conversion and K-shell double internal conversion has been calculated in this work.

The efficiency of the Super-e is calculated using a Monte-Carlo approach to sample the range of possible ejection energy and take off angles of the emitted particles according to the probability distribution of a particular process. For each set of ejection energy and take off angles, the trajectories of the charged particles in the magnetic field are determined by numerically solving the equations of motion for a charged particle in a magnetic field. The number of simulated particles that have appropriate trajectories to reach the detector is recorded. The ratio of simulated events from particles that reach the detector to the total number of generated trajectories then provides the efficiency. The solenoidal magnetic field inside the Super-e is well characterised [37].

The emission of single conversion electrons from a source is isotropic, due to the averaging out of any nuclear orientations due to the random alignment of the nuclei in a radioactive source. The efficiency of the Super-e to 624 keV conversion electrons at a magnetic field corresponding to a current of 3.10 A has been calculated in this work. The calculated efficiency,  $\eta_K$ , is

$$\eta_K = 0.0637.$$

The emission of double internal conversion electrons is different to that of single conversion electrons. Although there is no net alignment of the nuclei in the source, there is still an angular correlation in the separation angle between the two emitted electrons, in addition to the probability distribution in the energy of each electron. The double differential cross sections for the constituent multipole combinations and the total double differential cross section have been calculated and displayed in Section 3.4. The efficiencies of each multipole combination and the total efficiency of double internal conversion process have been calculated at a magnetic field corresponding to a current of 1.96 A, i.e. the magnetic field that centers the Super-e acceptance window on 293 keV charged particles corresponding to approximately equal energies for the two emitted conversion electrons. The results are displayed below with the efficiencies of the multipole combinations labelled by the particular transition combination and the efficiency of the total process labelled by the subscript KK.

$$\begin{aligned}\eta_{E1M3+M3E1} &= 6.484 \times 10^{-5} \\ \eta_{E2M2+M2E2} &= 9.822 \times 10^{-5} \\ \eta_{E3M1+M1E3} &= 1.748 \times 10^{-4} \\ \eta_{KK} &= 1.438 \times 10^{-4}\end{aligned}$$

It is shown above that the different multipole pathways have different efficiencies. This is a consequence of the different double differential cross sections of the processes. The Super-e preferentially selects those pairs with small separation angle and equal energy

---

sharing. The  $E3M1 + M1E3$  process has the greatest distribution of events in that region of the three multipole combinations and so has the highest efficiency.

## 4.4 Momentum selection

In addition to the magnetic field defining a range of possible acceptable trajectories and so the efficiency of the spectrometer, there is a strong and well-defined relationship between the energies of particles that traverse the baffles and reach the detector and the magnetic field produced by the solenoid.

The behaviour of the Super-e has been well characterised previously, [37, 38], by experiments using  $^{137}\text{Cs}$  and  $^{152}\text{Eu}$  sources, looking at 624 and 294 keV conversion electrons, respectively. It was found that the magnetic field and electron energy are correlated according to the formula:

$$B = \frac{C(r, \theta, \dots) k \sqrt{E^2 + 2m_0 c^2 E}}{m_0 c^2} \quad (4.1)$$

Where  $k$  is a constant, and  $C(r, \theta, \dots)$  is a coefficient which contains the response of the spectrometer with respect, primarily, to the baffle geometry but also the source placement and emittance [38].

Upper and lower bounds for  $C$  can be defined which maps out a region of acceptance on the electron energy-magnetic field plane. Events that fall within this region correspond to electrons that have traversed the Super-e and have deposited all their energy into the detector and are considered full or real events.

To detect real double conversion electron events, the background must be fully understood and suppressed as much as possible. More on the process of selecting out the real events from the background will be discovered in Section 5.4.



# Data Analysis

---

## 5.1 Event-by-Event Data

Event-by-Event data collection is a scheme wherein a set of correlated data are stored together as an ‘event’. For example, in the detection of a charged particle, the energy of the particle, the time of detection, and the strength of the magnetic field at the time of detection can be stored by the data acquisition system together as one event. This allows the sorting of data according certain properties called “gating”, so being able to obtain the spectrum of events of only those events that satisfy those particular conditions. In the sense of the example outlined above, one can project out the energy spectrum of particle detections when the magnetic field strength was between two values chosen as the limits of the “gate”.

## 5.2 Energy Gain Matching

Energy gain matching is an essential part of coordinating and using multi-detector arrays. The energy-channel response, the association of a particular energy to a particular channel in the spectrum, is set for each detector in the energy calibration of the detector. Such calibrations are often different between any two detectors. This response can change or drift over the course of an experiment. Any gain differences and or drifts have to be corrected for during the analysis of the collected data if one wishes one combine or compare data from pairs or arrays of detectors. Differences in the energy calibration arise both from differences in the detectors themselves and from differences in the pulse-processing electronics for each detector.

Energy gain matching is applying a correction, typically a constant or constant and linear shift to the energy spectrum of each detector to align the energy-channel response amongst the set of detectors. Typically, the array of detectors is exposed to a particular radiation or set of radiations, ones with well known energy values, which enable the alignment of the energy peaks in the histograms associated with the set of detectors.

### 5.3 Time Difference Matching

The time corresponding to each electron detection is recorded as part of the data in event-by-event data collection, whether the absolute time or a time value relative to some master timing signal. What is important in coincidence events is the difference in the time between detections of two radiations. In a similar fashion to the energy-channel relationship above, the timing calibrations for each detector must be adjusted to allow accurate comparison and collation of data among the set of detectors.

Time difference spectra are formed from the time differences among events between each pair of detectors. Coincidence events where the two detections were close in time will be positioned close to zero on the spectrum. This is the case only if the time calibrations between the two detectors are the same. A constant shift in the time response of one detector relative to the other will shift such events from the zero point.

In the presence of real time-correlated events, such as the emission of a positron-electron pair, one would expect to see a peak at some value on the time difference spectrum depending on the relative difference in the timing response between the two detectors along with their electronics modules. This peak exists as the events are time correlated. Uncorrelated events are uniformly distributed with respect to the time differences between detections.

Time difference matching involves the adjustment of the time spectrum of each detector, typically by a constant shift, to align the peaks of the time difference spectra between pairs of detectors. Typically, the time spectra are all aligned with the response of one particular detector, and made to align the peaks all to a particular channel defined as corresponding to zero time difference. Aligning the time difference spectra among the array of detectors is essential for the selecting of time correlated events out from a random background.

### 5.4 $B/B\rho$ Selection

As discussed in Chapter 4, legitimate events, those for which the electrons traversed the baffles and deposited all their energy in the detector, lie within a particular region on the Energy-Magnetic field strength plane. The limits of this region are defined by upper and lower values for the  $C$  coefficient, as seen in Equation 4.1, which defines the response of the spectrometer.

We can transform the plane by plotting the events onto an Energy- $C$  plane. The  $C$  coefficient is determined for each event by dividing the magnetic field strength value by the associated magnetic rigidity of the event,  $B\rho$ , which is a measure of how difficult it is to affect the trajectory of a charged particle by applying a magnetic field. The magnetic rigidity is determined the energy/charge ratio for a particle.

This transformation places all legitimate events into a horizontal band on the Energy- $C$  plane, parallel to the energy axis, confined with regard to the  $C$  axis by a lower and upper  $C$  value. The  $C$  coefficient is also referred to as the  $B/B\rho$  value. This relationship is visible in Figure 5.1.

We can then determine the limiting values for  $B/B\rho$  by looking at the projection of the

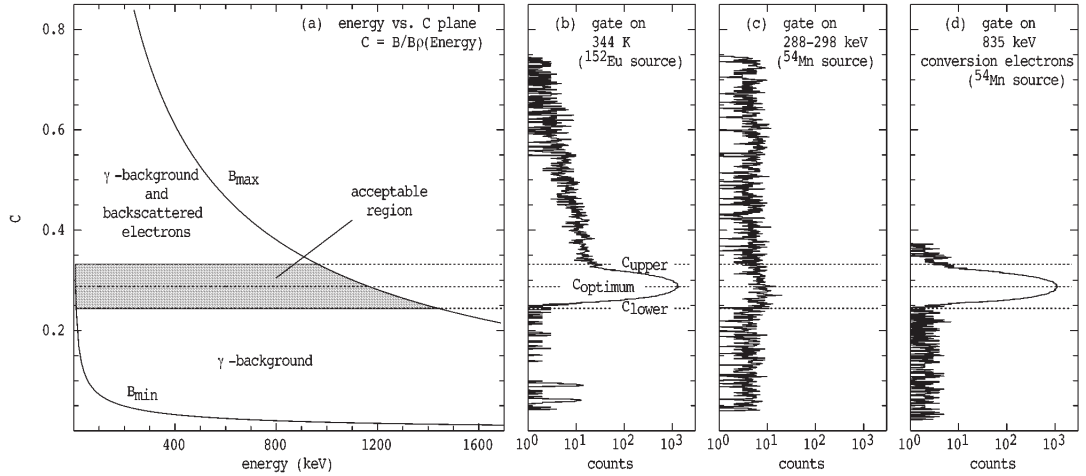


**Figure 5.1:** Plot of the Energy -  $B/B\rho$  plane. The region of legitimate events is within the horizontal band. Plot of the  $B/B\rho$  spectrum, those legitimate events are visible as a large peak above the continuous background. The limiting values of  $B/B\rho$  can be determined from the edges of the peak.

Energy -  $B/B\rho$  plane onto the  $B/B\rho$  axis. The limiting values of  $B/B\rho$  can then be observed from the edges of the response peak atop a spectrum of background events. This is visible in Figure 5.1

Backscatter events, events in which the electrons do not deposit their full energy into the detector, do not lie within this region. They lie in sweeping arcs, at a higher  $B/B\rho$  and lower energy than the legitimate events, outside the accepted region. The majority of these events can then be selected out and excluded in the data analysis.

Events which correspond to  $\gamma$ -ray detections will not be correlated in anyway to the magnetic field. They form an uniform background with respect to the magnetic field and like the backscatter events be largely filtered out from the data pool, except where they happen to fall in the acceptance range. In that case, they can be removed by a later subtraction process.

Those events which have  $B/B\rho$  values that lie outside the limiting values are not legitimate events. Therefore, a gate on the  $B/B\rho$  values of events is applied, with only events with a  $B/B\rho$  value within the determined limiting values being accepted during the sorting of the data.

## 5.5 Time Prompt Selection

The time difference spectra are used in the selection of time correlated events from a random event background. Intermingled with the real coincidence events, there will be random coincidences in the spectra from uncorrelated events that happen to trigger the detectors within the coincidence window. As these events are uncorrelated, it is expected that they would have a flat distribution with respect to the time difference between the events.

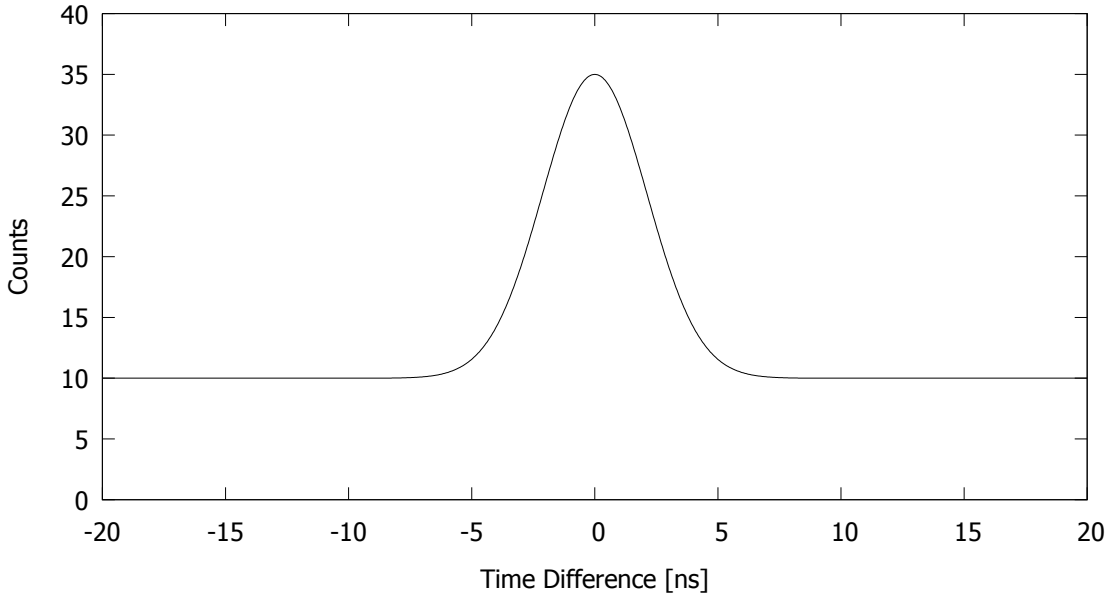


**Figure 5.2:** This is an example of a time difference spectrum where the central peak corresponds to events from time correlated processes while the broad flat wings are formed by the random background.

As discussed in Section 5.3, correlated events form a peak in the time difference spectrum. In the presence of uncorrelated processes, this will be positioned on top of the broad flat background. This is depicted in Figure 5.2.

Therefore it should be possible to separate out uncorrelated events (or the random coincidences) from the distribution of correlated events or coincidence events. This is done by excluding those events which lie outside the central peak. A gate is applied to the data set, with limiting values for the time differences set by determining the edges of the central peak, so that only those events which have values for the time difference inside the limiting values are accepted. However, while the majority of the random events will be excluded, the random background continues under the peak and so some random events will still be accepted.

## 5.6 Background Subtraction

These accepted spurious events that survive the time prompt selection can then be removed via the process of background subtraction. As discussed in Section 5.5, the random background is flat with respect to time difference as the events are uncorrelated. Therefore one can expect the random distribution is unchanged under the central peak compared with the flat spectrum outside the peak.

One can then sum the events that lie in the flat wings of the spectrum. This spectrum can then be averaged, and after scaling to the number of channels under the central time prompt peak, subtract them from the selected events. This approach removes the random

---

coincidence events from the selected real events. In order to minimise the impact of the error introduced to the spectrum through the background subtraction, it is important to take as wide a background section as possible.



# Experimental Procedure

---

The goal of the experiment undertaken here at the ANU using the Superconducting Spectrometer or Super-e was to experimentally measure the double conversion rate of K shell electrons relative to the single K conversion rate in the 662 keV M4 decay of  $^{137m}\text{Ba}$  or at least set a limit on the probability of the double internal conversion process.

The experiment consisted of two parts. One was an effort to measure the double conversion rate by looking for electron-electron coincidence events produced during the decay of  $^{137}\text{Cs}$  and measuring simultaneously the associated gamma-ray spectrum. The second part was a measurement of the K conversion electron spectrum emitted during the decay of  $^{137}\text{Cs}$  and also measuring the associated gamma-ray spectrum. The same detector arrangement was used for the gamma-ray measurements in both parts, enabling their use to normalise and compare the single-conversion and double-conversion spectra.

The intention was to then obtain an experimental value for the double internal K conversion rate relative to the single conversion rate by dividing the obtained number of K shell double internal conversion events by the number of K shell conversion events, scaling the value by the relative ratio of gamma-ray counts. The gamma-ray counts are then used as a proxy for time.

The state of interest in the experiments is the 662 keV excited state of  $^{137}\text{Ba}$ . This is populated in the  $\beta^-$  decay of  $^{137}\text{Cs}$ . A  $2.7 \mu\text{Ci}$   $^{137}\text{Cs}$  source was placed inside the Super-e and the emitted electrons were detected. The same source was used for both parts of the experiment. The experiment was run for a total time of around two weeks, including time to calibrate the detectors and organise the electronics.

Two magnetic field settings of the Super-e were used during the experiment. A current of 3.10 A was used for measurements of the 624 keV K conversion line and a current setting of 1.96 A was used for the measurements of the K shell double conversion spectrum. The current of 3.10 A corresponds to the maximal efficiency of the Super-e for 624 keV electrons and 1.96 A setting corresponds to an energy acceptance window centered on electron energy of 293 keV, the central energy of the K-shell double internal conversion process.

The magnetic field was automatically shifted between the two magnetic field settings throughout the experiment. This was done to measure the 624 keV K conversion line throughout the experiment in order to gain match the 6 Miel detectors and monitor any drifting of the energy calibrations during the experiment. For every 1000 seconds spent at the current setting of 1.96 A, 10 seconds were spent at 3.10 A.

The data was analysed according to the procedures outlined in Chapter 5. The energy calibrations of the detectors were aligned, as were the timing calibrations. The collected events were selected based on the  $B/B\rho$  values and time differences and the final spectrum was formed from background subtracted data.

The results of the experiment are presented and discussed in Chapter 7.

The experiment was intended to be repeated using a stronger  $^{137}\text{Cs}$  source, around  $27\ \mu\text{Ci}$ , in an effort to increase the number of observed counts of the double internal conversion process. The stronger source was to be procured from ANSTO however although a source of appropriate strength was made, it proved mechanically unstable and could not be used as the risk on contamination was very high.

# Experimental Results

Non coincidence (or “single”) electron events were recorded using the Miel detector array with the aim of measuring the K conversion line of  $^{137m}\text{Ba}$  at a magnetic field setting of 3.10 A. The associated  $\gamma$ -ray spectrum was recorded with the Apterix detector. As the electron events are single events, not coincidence events, legitimate events are selected by

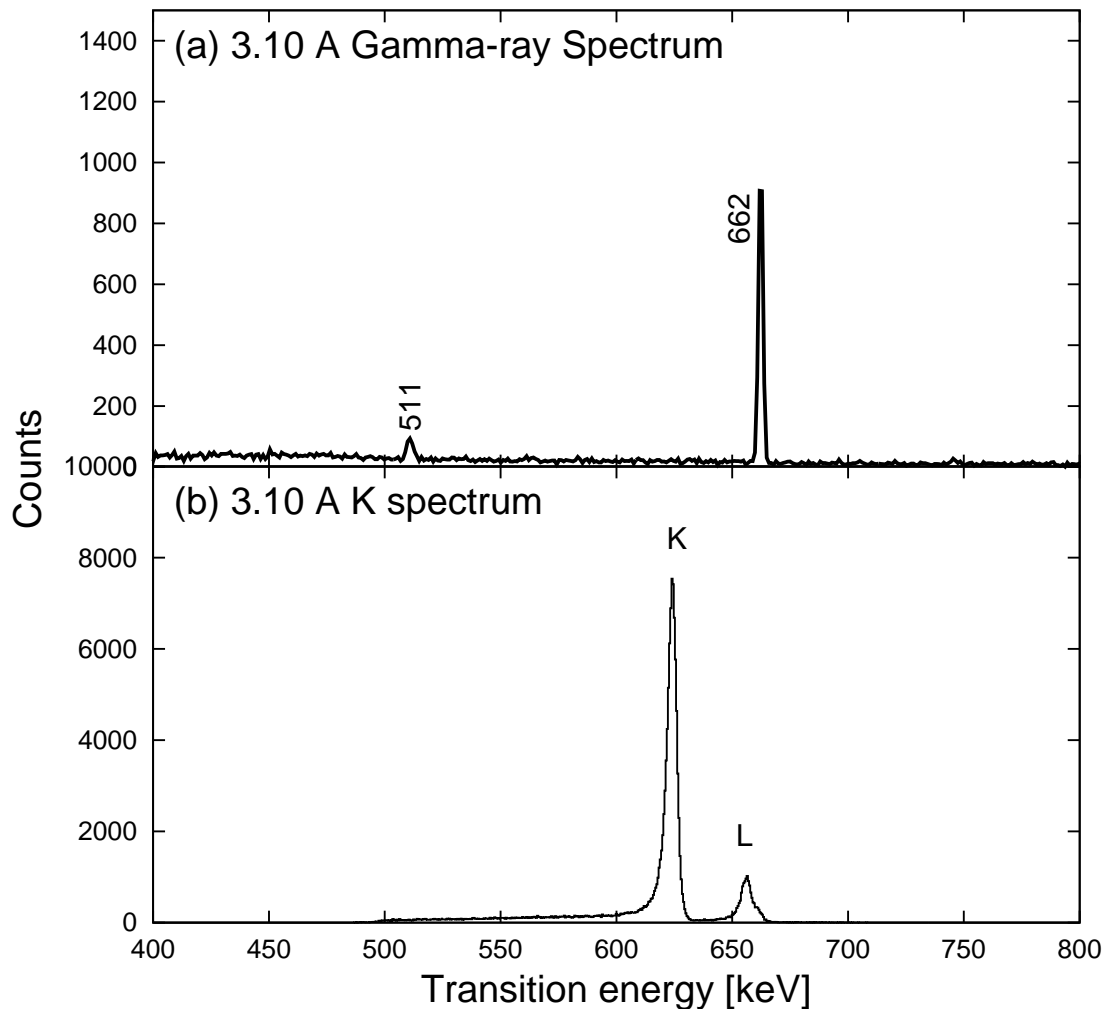
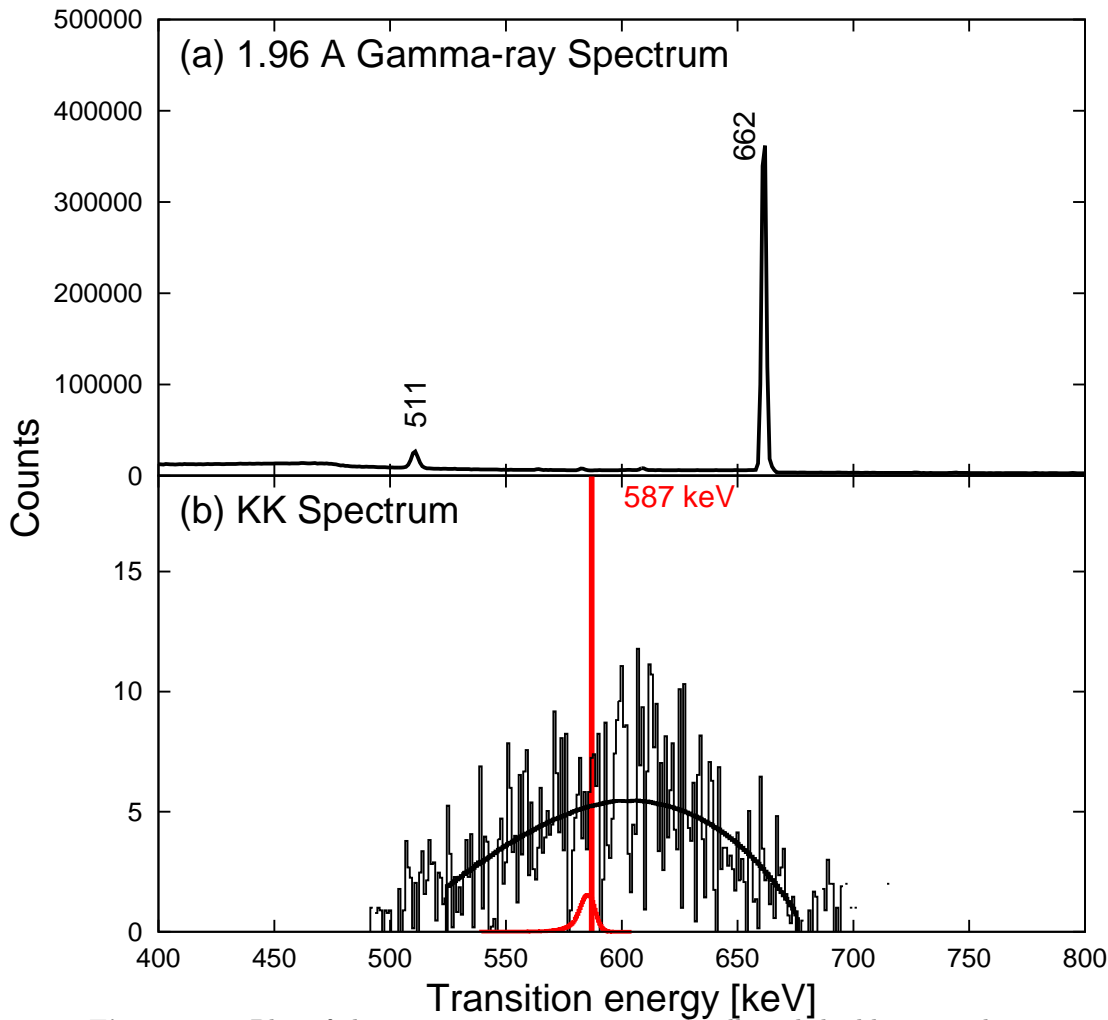


Figure 7.1: Plot of the gamma ray spectrum and collected conversion electron spectrum at a current setting of 3.10 A.



**Figure 7.2:** Plot of the gamma ray spectrum and collected double internal conversion electron spectrum at a current setting of 1.96 Å. The vertical red line denotes 587 keV, the expected peak location for K-shell double conversion events. The fitted background spectrum is plotted in black over the experimental spectrum.

the  $B/B\rho$  selection only. The obtained electron energy spectrum and  $\gamma$ -ray spectrum are plotted in Figure 7.1.

The  $\gamma$ -ray spectrum shows a strong peak at 662 keV, the  $\gamma$ -ray decay line of  $^{137m}\text{Ba}$ . The conversion electron spectrum shows two peaks: the K conversion line at 624 keV, the focus of this measurement, and a secondary peak at 656 keV corresponding to L-shell conversion. The number of events above the background in the  $\gamma$ -ray peak and the K conversion line are obtained.

$$\begin{aligned} N_K &= 83314(2499) \\ \gamma_K &= 2374(81) \end{aligned}$$

Electron-electron coincidence events were examined with the Miel detector array at a magnetic field setting of 1.96 Å and the corresponding spectrum of  $\gamma$ -ray events was recorded with the Apterix detector, in the same arrangement as in the 3.10 Å measurement.

---

The electron-electron events were selected from the background using  $B/B\rho$  selection, time prompt selection and with background subtraction from the time difference spectrum as outlined in Chapter 5.

Each electron coincidence event consists of two electron detections, each in a separate segment of the Miel detector array, each with a corresponding energy. The energies of pair of detections are summed to form an energy summed spectrum of the electron-electron coincidence events. This spectrum is plotted in Figure 7.2 along with the  $\gamma$ -ray spectrum recorded at the magnetic field setting of 1.96 A.

Like in Figure 7.1, the  $\gamma$ -ray spectrum is dominated by the 662 keV peak, the peak of interest. There are no significant peaks in the simultaneously obtained summed electron energy spectrum. The number of 662 keV gamma ray events,  $\gamma_{KK}$  is

$$\gamma_{KK} = 920756(59849)$$

The summed energy of two K electron converted via double internal conversion in the 662 keV transition is 587 keV, corresponding to 662 keV minus two times the binding energy of the K shell electrons. The presence of a peak at 587 keV in the summed electron energy spectrum would be characteristic of double internal conversion. No such peak is present in Figure 7.2. We can however compare the experimental spectrum, Figure 7.2, to the theoretical prediction and set an experimentally derived limit on the rate of double internal conversion of the K shell to the rate of K conversion in the decay of  $^{137m}\text{Ba}$ .

The presence of the 511-keV peak in both Figures 7.1, 7.2 suggests the presence of residual activity inside the Super-e. The 511-keV peak corresponds to the rest mass energy of an electron and represents the gamma ray produced by the annihilation of a positron. The 662 keV transition does not have sufficient energy to pair produce a positron so the existence of the 511 peak in the gamma ray spectra strongly suggests the presence of some other radioactive material inside the Super-e.

The expected number of recorded double internal K conversion events by the Super-e is given by Equation 7.1 where  $N_{KK}$  is the expected number of counts,  $\gamma_{KK}$  and  $\gamma_K$  are the number of detected gamma ray events for the 1.96 A setting and 3.10 A setting respectively,  $\eta_{KK}$  is the efficiency of the Super-e for double internal K conversion at 1.96 A,  $\eta_K$  is the efficiency of the Super-e for 624 keV K conversion at 3.10 A,  $P_{KK}/P_K$  is the rate of double K internal conversion to single K conversion, and  $N_K$  is the detected number of K conversion events.

$$N_{KK} = \left( \frac{\gamma_{KK}}{\gamma_K} \right) \left( \frac{\eta_{KK}}{\eta_K} \right) \left( \frac{P_{KK}}{P_K} \right) N_K \quad (7.1)$$

The factor of  $(\gamma_{KK}/\gamma_K)$  is used a proxy for the measurement time to normalise the relative number of K conversion counts to the K shell double internal conversion counts and the  $(\eta_{KK}/\eta_K)$  factor takes into account the different efficiencies of the two processes in the Super-e.

The efficiency of the Super-e with respect to double internal conversion at a magnetic field setting of 1.96 A and single K conversion at a magnetic field setting of 3.10 A has been

calculated in Section 4.3. The efficiencies are given below.

$$\begin{aligned}\eta_K &= 0.0673 \\ \eta_{KK} &= 1.438 \times 10^{-4}\end{aligned}$$

Using Equation 7.1 and the number of measured  $\gamma$ -rays at 1.96 Å and 3.10 Å, along with the efficiencies and the number of measured K-conversion events, we can calculate the expected number of measured double conversion events and compare with the experimental results.

The theoretical rate of double internal conversion of the K shell is  $P_{KK}/P_K = 1.315 \times 10^{-6}$ , calculated in Section 3.4. This gives an expected number of measured counts of

$$N_{KK} = 0.091$$

This is consistent with the experimental results, as the theory predicts no significant peak.

A previous measurement on double internal conversion was undertaken in 1971 by Ljubicić et al. [28]. This was a direct measurement of electron coincidence events in conjunction with an X-ray from the filling of the K shell vacancies of the atom. The obtained an experimental limit of  $18(5) \times 10^{-5}$  for the rate of double K-shell electron ejection relative to the K-shell conversion rate for coincidence electrons of energy between 115 to 472 keV. It is unknown how much of this measured rate is due to the contribution of alternative K-shell electron ejection mechanisms. If we assume the obtained rate is solely due to the double internal conversion process, we obtain an expected number of counts for this experiment of 27 counts. A peak containing this many counts is plotted in red in Figure 7.2. A peak this size is in agreement with the experimentally observed spectrum.

We can also use Equation 7.1 to calculate a limit of the K shell double internal conversion process in the 662 M4 transition of  $^{137m}\text{Ba}$ . The background has a height of 5 counts in the region of 587 keV. The statistical uncertainty we would then expect in the spectrum is  $\sqrt{5} = 2.24$ .

The line shape of a double internal conversion peak has been derived from looking at the line shape of the single conversion electron spectrum. However, the expected full width at half maximum of the double conversion peak shape is increased by a factor of  $\sqrt{2}$  to account for the fact that the peak is created from the addition of two spectra.

Taking the statistical uncertainty in the spectrum as the peak height of the limiting spectral peak, we obtain a peak containing 25 counts.

A maximal estimate of the measured number of KK events in the spectrum in Figure 7.2 is then 25 counts, leading to an experimentally obtained limiting value of  $P_{KK}/P_K$  of  $20.8 \times 10^{-5}$ .

If the stronger  $^{137}\text{Cs}$  source was available and used as the source in the current experiment then we would expect an increase in the number of expected double internal conversion counts by a factor of 10, to give an expected number of  $N_{KK} = 0.9$ . In order to observe a significant number of double internal conversion events, the experiment would need to run for greater than 40 weeks.

# Conclusion and Outlook

---

## 8.1 Conclusion

There have been many measurements of the rate of double K-shell electron ejection in  $^{137}\text{Ba}$ , some of which are displayed in Table 2.2. All of these measurements are of the total rate of the ejection of two K-shell electrons from the atom, not of double internal conversion of K-shell electrons. Heretofore, The properties of double internal conversion have been unknown, especially in relation with the other dual electron ejection mechanisms.

No theoretical calculation of the expected rate of double internal conversion in nuclear transitions has been done in the literature using the consistent theory put forward by Grechukhin [12]. The energy and angular distributions of the process has never been calculated nor has been total rate of the double internal process.

In this work, the theoretical model for double internal conversion produced by Grechukhin has been explored. The theoretical model was extended to develop the expression for the double differential cross section. A general computer program for the calculation of the double internal conversion rate for a nuclear transition was developed from the theoretical model. This program was applied to the 662 keV transition in  $^{137m}\text{Ba}$ . The double differential cross section for double internal conversion was calculated, obtaining the energy and angular distribution information about the double internal conversion process for the first time. These calculations are presented in Chapter 3. In addition, the total expected double internal conversion rate was calculated to be  $P_{KK}/P_K = 1.32 \times 10^{-6}$  relative to the rate of single conversion in  $^{137m}\text{Ba}$ . This calculated rate is very similar to the experimentally observed double gamma emission rate in  $^{137}\text{Ba}$  of  $P_{\gamma\gamma}/P_\gamma = 2.06(37) \times 10^{-6}$ .

Using the theoretical calculations of the double differential cross section, we could calculate the efficiency of the super-e to the double internal conversion process, allowing us to undertake an experiment to observe this process experimentally.

An experiment was performed using the Superconducting electron spectrometer, or Super-e, here at the ANU. Electron-electron coincidences and the K conversion electrons were observed. The experimental results are in agreement with the theoretical predictions and an experimental limiting value of the double internal conversion rate has been established. The independent maximal experimental limit obtained from the experiment is  $P_{KK}/P_K = 20.8 \times 10^{-5}$ .

Unfortunately, due to the expected rarity of the double internal conversion process and the current experimental apparatus, experimentally observing double internal conversion

in  $^{137}\text{Ba}$  is not expected. There is however, significant room for future work in this area.

In addition, the level of the background counts in the current experimental setup has been measured which is important for any future work as it sets the significance threshold that future experimental observations will have to surpass.

## 8.2 Future Direction

In order to observe double internal conversion in the decay of  $^{137m}\text{Ba}$  experimentally, the efficiency of the experimental set up must be improved. This can be done via the addition of another set of detectors and baffle element on the short end of the Super-e solenoid. This would allow for the detection of events with a large angular separation. As the majority of double internal conversion events in  $^{137m}\text{Ba}$  are at large angles, this would improve the efficiency and could enable a successful experimental observation of double internal conversion.

Secondly, double internal conversion could be investigated in a transition of different nucleus, for example the M4 transition in the decay of  $^{207}\text{Bi}$ . The different multipole combinations have different efficiencies in the Super-e, and so it is possible that double internal conversion could be observed more easily in  $^{207}\text{Bi}$ .

The model that has been developed is a general model, for any nucleus and any non-mixed transition, as long as the nuclear transition matrix elements and conversion coefficients can be calculated. Therefore, in principle, we could investigate and characterise double internal conversion in any decay transition.

The operation of the Super-e with a source is independent of the accelerator schedule. Therefore, we can in principle run the Super-e continuously allowing for long experimental times.

---

# Bibliography

---

- [1] W. D. Hamilton, *The Electromagnetic Interaction in Nuclear Spectroscopy* (North Holland, 1975)
- [2] D. H. Wilkinson, and D. E. Alburger, Phys. Rev. C **5**, 719 (1972)
- [3] H. J. Nagy, K. E. Brady, and G. Schupp, Phys. Rev. C **38**, 2818 (1988)
- [4] C Walz, H. Schiet, N. Pietralla, T. Aumann, R. Lefol, and V. Yu. Ponomarev, Nature **526**, 406 (2015)
- [5] C. Walz, PhD, Darmstadt, 2014
- [6] J. Kramp, D. Habs, R. Kroth, M. Music, J. Schirmer and D. Schwalm, Nucl. Phys. A **474**, 412 (1987)
- [7] M. E. Rose, Phys. Rev. **76**, 678 (1949)
- [8] J. Eichler, and G. Jacob, Z. Phys. **157**, 286 (1959)
- [9] J. Eichler, Z. Phys. **160**, 333 (1960)
- [10] D. P. Grechukhin, Nuclear Physics **35**, 98 (1962)
- [11] D. P. Grechukhin, J. Nucl. Phys. (U.S.S.R.) **4**, 42 (1966)
- [12] D. P. Grechukhin, J. Nucl. Phys. (U.S.S.R.) **4**, 497 (1966)
- [13] E. G. Drukarev, Z. Phys. A **359**, 133 (1997)
- [14] T. Mukoyama and S. Shimizu, Phys. Rev. C **11**, 1353 (1975)
- [15] T. Mukoyama and S. Shimizu, Phys. Rev. C **13**, 377 (1976)
- [16] M. S. Freedman, Annu. Rev. Nucl. Sci. **24**, 209, (1974)
- [17] E. L. Feinberg, Yad. Fiz. **1**, 612 (1965) [Sov. J. Nucl. Phys. **1**, 438 (1965)]
- [18] M. A. Listengarten, Vestn. Leningr. Univ., Fiz. Khim. **16**, 142 (1962)
- [19] W. Beusch, Helv. Phys. Acta **33**, 363 (1960)
- [20] G. J. McCallum, P. A. Bromly, and J. A. Kuehner, Nucl. Phys. **20**, 382 (1960)
- [21] B. A. Watson, T. T. Bardin, J. A. Becker, and T. R. Fisher, Phys. Rev. Lett. **35**, 1333 (1975)
- [22] J. Schirmer, D. Habs, R. Kroth, N. Kwong, D. Schwalm, and M. Zirnbauer, Phys. Rev. Lett. **53**, 1897 (1984)
- [23] H. J. Nagy, G. Schupp, and P. R. Hurst, Phys. Rev. C **11**, 205 (1975)

- [24] C. W. E. van Eijk, J. Wijnhorst, and M. A. Popelier, Phys. Rev. C **19**, 1047 (1979)
- [25] J. P. Briand, P. Chevallier, A. Johnson, J. P. Rozet, M. Travernier, and A. Touati in *Proceedings of the Internationaal Conference on Inner Shell Ionization Phenomena, Atlanta, 1972*, edited by R. W. Fink *et al.* (Georgia Institute of Technology, Atlanta; Emory University, Atlanta, Georgia, 1973)
- [26] R. Vukanović, L. Samuelsson, M. Migahed, L. Westerberg, and L. O. Edvardson, Phys. Lett. **29B**, 576 (1969)
- [27] K. Knauf, H. Sommer, and H. Klewe-Nebenius, Z. Phys. **197**, 101 (1966)
- [28] A. Ljubicić, M. Jurcevic, K. Ilakovac, and B. Hrastnik, Phys. Rev. C **3**, 831 (1971)
- [29] J. P. Briand, P. Chevallier, A. Johnson, J. P. Rozet, M. Travernier, and A. Touati, Phys. Lett. **49A**, 51 (1974)
- [30] H. J. Nagy and G. Schupp, Phys. Rev. C **32**, 2043 (1985)
- [31] D. P. Grechukhin, JETP **32**, 1036 (1957), Soviet Phys. JETP **5**, 846 (1957)
- [32] H. C. Pauli, and U. Raff, Computer Physics Communications **9**, 392 (1975)
- [33] M. E. Rose, *Multipole Fields* (John Wiley & Sons, 1955)
- [34] A. Surzhykov, A. Volotka, F. Fratini, J. P. Santos, P. Indelicato, G. Plunien, Th. Sthlker, and S. Fritzsch, Phys. Rev. A **81**, 042510 (2010)
- [35] L. Safari, P. Amaro, J. P. Santos, and F. Fratini, Phys. Rev. A **90**, 014502 (2014)
- [36] V. G. Soloviev, *Theory of Atomic Nuclei: Quasiparticles and Phonons* (IOP Publishing, 1992)
- [37] T. Kibédi, G. D. Dracoulis, and A. P. Byrne, Nuclear Instruments and Methods in Physics Research A **294**, 523 (1990)
- [38] T. Kibédi, M. Kerr, E. B. Norman, G. D. Dracoulis, and A. P. Byrne, The Astrophysical Journal **489**, 951 (1997)